THE JOURNAL OF PHYSICAL CHEMISTRY C

Article

pubs.acs.org/JPCC

Kinetic and Theoretical Insights into the Mechanism of Alkanol Dehydration on Solid Brønsted Acid Catalysts

William Knaeble and Enrique Iglesia*

Department of Chemical and Biomolecular Engineering University of California, Berkeley, California 94720, United States

Supporting Information

ABSTRACT: Elementary steps that mediate ethanol dehydration to alkenes and ethers are determined here from rate and selectivity data on solid acids of diverse acid strength and known structure and free energies derived from density functional theory (DFT). Measured ethene and ether formation rates that differed from those expected from accepted monomolecular and bimolecular routes led to our systematic enumeration of plausible dehydration routes and to a rigorous assessment of their contributions to the products formed. H-bonded monomers, protonated alkanol dimers, and alkoxides are the prevalent bound intermediates at conditions relevant to the practice of dehydration catalysis. We conclude that direct and sequential (alkoxide-mediated) routes contribute to ether formation via S_N2-type reactions; alkenes form preferentially from sequential routes via monomolecular and bimolecular syn-E2-type eliminations; and alkoxides form via bimolecular S_N2-type substitutions. The prevalence of these elementary steps and their kinetic relevance are consistent with measured kinetic and thermodynamic parameters, which agree with values from DFT-derived free energies and with the effects of acid strength on rates, selectivities, and rate constants; such effects reflect the relative charges in transition states and their relevant precursors. Dehydration turnover rates, but not selectivities, depend on acid strength because transition states are more highly charged than their relevant precursors, but similar in charge for transition states that mediate the competing pathways responsible for selectivity.

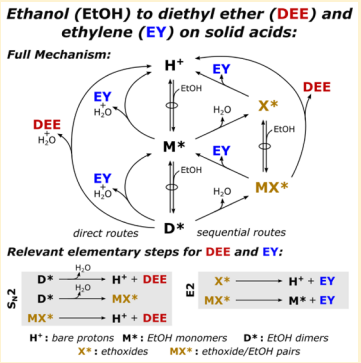

1. INTRODUCTION

The recent increase in demand for renewable carbon sources[1] has led to a concomitant increase in ethanol (EtOH) production (10-fold from 1995 to 2014 in the U.S.[2]). EtOH has also emerged as an attractive feedstock to produce hydrocarbon fuels (via deoxygenation−oligomerization)[1] and chemical intermediates, such as ethylene (EY) and diethyl ether (DEE) (via dehydration on solid Brønsted acids).[3−7] EtOH dehydration rates and selectivities have been widely reported,[3−5,7−14] but only on solids with acid sites uncertain in number, type, location, or local structure, obfuscating reactivity comparisons among catalysts and mechanistic elucidation. In the absence of clear mechanistic insights, the role of acid strength and confinement on reactivity (as turnover rates) and selectivity, required for systematic catalyst improvements, has remained unclear and not rigorously demonstrated.

Tungsten polyoxometalate (POM) clusters with Keggin structures and charge-balancing protons ($H_{8-n}X^{n+}W_{12}O_{40}$) are used in practice to convert EtOH to EY.[15−17] These solids also represent a family of Brønsted acids with uniform and well-defined atomic arrangements and diverse chemical composition (X^{n+} = P^{5+}, Si^{4+}, Al^{3+}, Co^{2+}).[18] The identity of the central atom (X) influences acid strength and consequently the reactivity of the protons, through changes in their number and in the stability of the conjugate anion formed upon deprotonation of the solid acid.[19] Deprotonation energies (DPEs) reflect the energy required to heterolytically cleave a proton from its conjugate base, thus providing a rigorous and probe-independent measure of acid strength; their magnitude can be determined using density functional theory (DFT) because of the known and stable structure of these catalysts.[19,20]

Methanol (MeOH) can form only bimolecular dehydration products (dimethyl ether), while larger 1-butanol and 2-butanol reactants (BuOH) predominantly convert via monomolecular routes (to butenes) on Keggin POM clusters and acid forms of zeolites.[19−22] Consequently, these reactants cannot probe reactions (and transition states) of different molecularity involved in the two dehydration paths. EtOH reacts via monomolecular (to EY) and bimolecular (to DEE) routes on Brønsted acids at conditions relevant to the practice of dehydration catalysis, thus providing a unique opportunity to explore these mechanisms in concert.

Here, alcohol dehydration routes to alkenes and ethers are explored by combining EtOH rate and selectivity data on Brønsted acids of known structure and a broad range of acid strength ($H_{8-n}X^{n+}W_{12}O_{40}$) with density functional theory (DFT) treatments of acid strength and plausible elementary steps. Total EtOH dehydration rate data can be made consistent with several mechanistic interpretations, including one that is often implicated, in which monomolecular and

Received: November 13, 2015
Revised: December 20, 2015
Published: January 21, 2016

© 2016 American Chemical Society

DOI: 10.1021/acs.jpcc.5b11127
J. Phys. Chem. C 2016, 120, 3371−3389

bimolecular elementary steps mediate EY and DEE formation, respectively. The measured ratios of formation rates (r_{DEE}/r_{EY}), however, are inconsistent with these accepted pathways. It is such inconsistencies that motivate our reassessment of alkanol dehydration pathways. Such an assessment, if it is to be rigorous and complete, requires that we enumerate each plausible sequence of elementary steps, that we calculate their rates through accurate estimates of Gibbs free energies for all intermediates and transition states (instead of only their enthalpies), and that we systematically evaluate their respective contributions to measured rates, using protocols based on sensitivity and rate-of-production analyses. These protocols replace the customary visual inspection of graphical reaction coordinate depictions with a more complete theoretical framework suitable for quantitative comparisons. Such strategies are employed here, using constants predicted from DFT-derived free energies, to reduce the number of relevant species and connecting reactions by retaining only those consequential for the formation of EY and DEE at conditions relevant to the practice of catalytic dehydration. The resulting reduced mechanism is consistent with all measured rates and selectivities; the measured rate and equilibrium constants agree well with those obtained from DFT-derived free energies on all POM acids.

2. METHODS

2.1. Catalyst Synthesis. Catalyst synthesis details have been reported elsewhere.[23] $H_3PW_{12}O_{40}$ (Sigma-Aldrich; reagent grade; CAS #12501-23-4), $H_4SiW_{12}O_{40}$ (Aldrich; >99.9%; CAS #12027-43-9), $H_5AlW_{12}O_{40}$,[24] and $H_6CoW_{12}O_{40}$[25,26] were dispersed onto colloidal SiO_2 (Cab-O-Sil HS-5; 310 $m^2\ g^{-1}$; 1.5 $cm^3\ g^{-1}$ pore volume) using incipient wetness impregnation at 0.04 POM $[nm\text{-}SiO_2]^{-2}$ surface densities (~5.0% wt), unless noted otherwise. SiO_2-supported POM clusters are denoted here as "H_nXW/SiO_2", where n is proton stoichiometry. ^{31}P-MAS NMR spectra showed that H_3PW Keggin structures were unchanged upon dispersion onto the SiO_2 support and after use in catalysis;[23] transmission electron micrographs showed that POM clusters were present as isolated clusters with two-dimensional aggregates as minority species at these surface densities.[23]

2.2. Dehydration Rate Measurements and Titrations with 2,6-Di-*tert*-butylpyridine. Ethanol (EtOH) dehydration rates and selectivities were measured on samples (0.02−0.7 g) held within a packed-bed stainless steel tubular reactor (3/8 in. O.D.) with plug-flow hydrodynamics. Reactor temperatures were controlled using a resistively heated furnace and measured with two K-type thermocouples (Omega; ±0.2 K), one held within a 1/16 in. stainless steel sheath aligned axially along the bed and another held against the external reactor wall. Pressure was controlled with a backpressure regulator (Equilbar, model EB1LF2).

Liquid ethanol (EtOH; Sigma-Aldrich; ≥99.5%, anhydrous) was evaporated into a flowing He stream (UHP Praxair) using a syringe pump (Cole-Palmer 74900 Series). All transfer lines were kept at 423 K to prevent condensation of reactants, products, and titrants. He flow rates were metered using electronic mass flow controllers (Porter, model 201). Molar flow rates of EtOH and He were controlled to give the desired EtOH pressures and maintain low EtOH conversions (<15%). Reactant and product concentrations were measured by gas chromatography using flame ionization detection (Agilent 6890N GC; 50 m HP-1 column). Diethyl ether (DEE) and ethylene (EY) were the only products detected on all catalysts; no products were detected when reactant streams were exposed to empty reactors; and gas chromatography measurements of reactor effluent streams using temperature conductivity detection (Agilent 6890N GC; 50 m HP-1 column) did not show any additional products besides water. Moderate catalyst deactivation was observed on H_5AlW/SiO_2 (<25% after 18 ks time on stream) and H_6CoW/SiO_2 (<50% after 18 ks time on stream) catalysts. In such cases, rates were corrected for any intervening deactivation by periodic rate measurements at a reference condition (1.0 kPa EtOH).

The number of Brønsted acid sites (H^+) accessible during catalysis was measured by titration with a noncoordinating base during catalysis. Titrations were conducted by dissolving 2,6-di-*tert*-butylpyridine (DTBP, Aldrich; >97%; CAS #585-48-8) in EtOH (0.024−0.086% mol) and introducing the mixture into a He stream (UHP Praxair) to give 0.45 or 2.6 Pa DTBP pressures. EtOH dehydration rates and DTBP uptakes were determined from EtOH, EY, DEE, and DTBP concentrations in the reactor effluent. The number of DTBP molecules required to fully suppress dehydration rates was used to determine the number of H^+ responsible for measured rates.[27]

2.3. Computational Methods. Periodic gradient-corrected density functional theory (DFT) was used as implemented in the Vienna ab initio simulation package (VASP)[28−31] to calculate structures and energies of gaseous reactants and products and of bound stable intermediates and transition states (TS) on Keggin POM clusters ($H_{8-n}X^{n+}W_{12}O_{40}$) with different central atoms (X^{n+} = P^{5+}, Si^{4+}, Al^{3+}, and Co^{2+}). A periodic plane-wave basis-set expansion to a cutoff energy of 396.0 eV was used to represent the wave functions for valence electrons. The projector augmented-wave method (PAW)[32,33] was used to describe electron−core interactions. The Perdew−Wang (PW91)[34] functional was used to calculate exchange and correlation energies within the generalized-gradient approximation. Electronic structures were converged self-consistently to energies within 1×10^{-6} eV with a $1 \times 1 \times 1$ Monkhorst−Pack[35] sampling of the first Brillouin zone (k-point mesh) and specified integer band occupancies (appropriate for the nonperiodic molecular systems treated here) for each step in both structural optimizations and single-point calculations. All calculations for POM clusters with Co central atoms were performed with spin polarization and three unpaired electrons, corresponding to the Co^{2+} electronic configurations. Spin-restricted calculations were used for all other compositions.

The structures and energies of Keggin clusters (~1.2 nm diameter) and gaseous molecules were calculated by placing them at the center of a cubic unit cell with an edge length of 3 nm to provide an intervening vacuum region sufficiently large to prevent interactions among clusters in adjacent unit cells.[20,36,37] Calculations of charged species were performed with uniform background charges to maintain neutral unit cells, and the resulting energies were corrected using methods[38] implemented in VASP. Long-range interactions among atoms in neighboring unit cells in charged and neutral systems were corrected using dipole and quadrupole moments, with the center of charge located at the center of the unit cell. Structures were relaxed until forces on all atoms were within 0.05 eV $Å^{-1}$. The charges at individual atoms were determined by Löwdin population analyses,[39,40] after transforming converged wave functions of optimized structures into a set of localized quasiatomic orbitals (QUAMBO).[41−44]

DOI: 10.1021/acs.jpcc.5b11127
J. Phys. Chem. C 2016, 120, 3371−3389

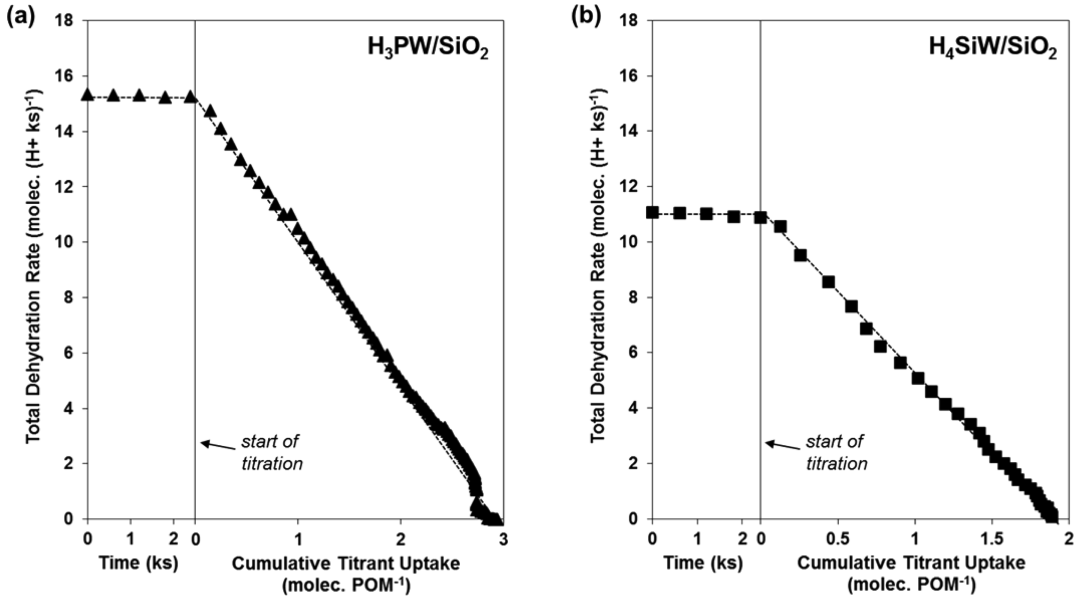

Figure 1. Total dehydration turnover rates on (a) H_3PW/SiO_2 and (b) H_4SiW/SiO_2 as a function of time before 2,6-di-*tert*-butylpyridine injection (1.0 kPa EtOH) and as a function of cumulative titrant uptake (1 kPa EtOH, 0.3 Pa 2,6-di-*tert*-butylpyridine) at 409 K.

Table 1. Number of Accessible H^+ per POM Cluster Measured by Chemical Titration with 2,6-Di-*tert*-butylpyridine[a] during Ethanol Dehydration[b] on $H_nXW_{12}O_{40}/SiO_2$ (X = P, Si, Al, and Co) Catalysts

catalyst	POM content (% wt.)	POM surface density (POM $(nm^2\ SiO_2)^{-1}$)	accessible H^+ (per POM)	H^+ surface density (H^+ $(nm^2\ SiO_2)^{-1}$)
$H_3PW_{12}O_{40}$	5	0.034	2.5	0.09
	10	0.067	2.9	0.18
$H_4SiW_{12}O_{40}$	5	0.034	1.9	0.06
$H_5AlW_{12}O_{40}$	5	0.033	2.7	0.09
$H_6CoW_{12}O_{40}$	5	0.039	2.5	0.10

[a]Assuming a 1:1 DTBP:H^+ adsorption stoichiometry [b]$H_3PW_{12}O_{40}/SiO_2$ (5 wt %):0.08 kPa EtOH, 409 K. Other catalysts: 1 kPa EtOH, 409 K.

Minimum energy reaction paths were calculated using nudged elastic band (NEB) methods[45] with structures converged to energies within 1×10^{-4} eV and forces to within 0.3 eV $Å^{-1}$ to identify starting structures for TS structures and reaction modes. NEB TS structures were refined using Dimer calculations[46] with convergence criteria of within 1×10^{-6} eV for energies and 0.05 eV $Å^{-1}$ for forces on each atom. The structures of bound intermediate and TS were determined at the proton location labeled H_B in Figure 3 for $H_3PW_{12}O_{40}$.

Deprotonation energies (DPEs) are defined as the energy of an isolated proton (H^+) and a structurally relaxed and isolated anion (A^-) relative to that for an intact acid (HA)

$$\mathrm{DPE} = E^{H^+} + E^{A^-} - E^{HA} \quad (1)$$

DPE values reported are for protons located at the bridging O atom labeled as H_B in Figure 3 for $H_3PW_{12}O_{40}$.

For all reactant, product, and transition states reported here, enthalpies

$$H = E_0 + \mathrm{ZPVE} + H_{vib} + H_{trans} + H_{rot} \quad (2)$$

and free energies

$$G = E_0 + \mathrm{ZPVE} + G_{vib} + G_{trans} + G_{rot} \quad (3)$$

include contributions from electronic energies (E_0), zero-point vibrational energies (ZPVEs), vibrational enthalpies and free energies (H_{vib} and G_{vib}), and for gaseous molecules their translational and rotational enthalpies (H_{trans} and H_{rot}) and free energies (G_{trans} and G_{rot}). ZPVE, H_{vib}, and G_{vib} values were determined from the frequencies in optimized structures.[47] Low-frequency modes of weakly bound adsorbates give rise to significant inaccuracies in vibrational contributions to free energies;[37] they were excluded from Gibbs free energy calculations. These modes were assumed instead to retain a fraction (0.7) of the translational and rotational entropies estimated by statistical mechanics for gaseous EtOH (3.15×10^{-4} eV/K), which was shown to provide accurate estimates of adsorption entropies for adsorbed molecules on oxide surfaces.[48] H_{trans}, H_{rot}, G_{trans}, and G_{rot} values for gaseous species were computed using statistical mechanics formalisms.[47]

Rate constants for elementary steps were estimated from differences in free energies between each TS and its relevant precursors ($\Delta G^{\ddagger}$)

$$k = \frac{k_B T}{h} \exp\left(-\frac{\Delta G^{\ddagger}}{RT}\right) \quad (4)$$

where k_B is Boltzmann's constant and h is Planck's constant.[49,50]

3. RESULTS AND DISCUSSION

EtOH dehydration rates were measured on silica-supported Keggin POM clusters (H_nXW/SiO_2) with different central atoms (X = P, Si, Al, and Co) at 409 K. EtOH formed bimolecular and monomolecular dehydration products (DEE and EY, respectively) at all conditions and on all catalysts. Total dehydration rates are defined here as the combined molar rates

DOI: 10.1021/acs.jpcc.5b11127
J. Phys. Chem. C 2016, 120, 3371−3389

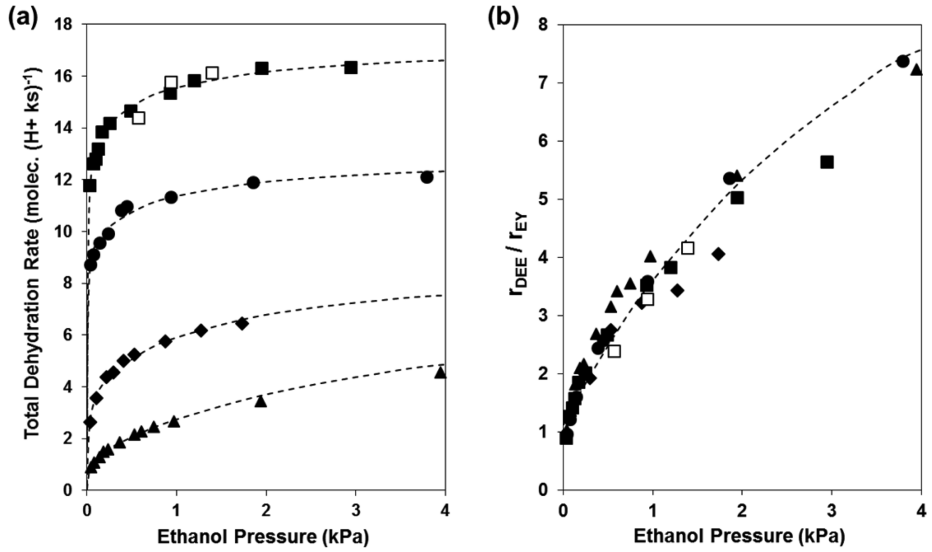

Figure 2. Measured (a) total EtOH dehydration turnover rates and (b) ratios of the rate of DEE formation to the rate of EY formation (r_{DEE}/r_{EY}) as functions of EtOH pressure (kPa) on H_3PW/SiO_2 (H^+ [nm-SiO_2]$^{-2}$ = 0.09 (■) and 0.18 (□)), H_4SiW/SiO_2 (●), H_5AlW/SiO_2 (◆), and H_6CoW/SiO_2 (▲) (reaction conditions: 409 K, 0.02−4 kPa EtOH). Dashed lines represent the regression of the data to the functional form of eqs 15 and 16.

Scheme 1. Plausible Sequences of Elementary Steps for the Formation of EY and DEE from EtOH on Brønsted Acid Sites[a]

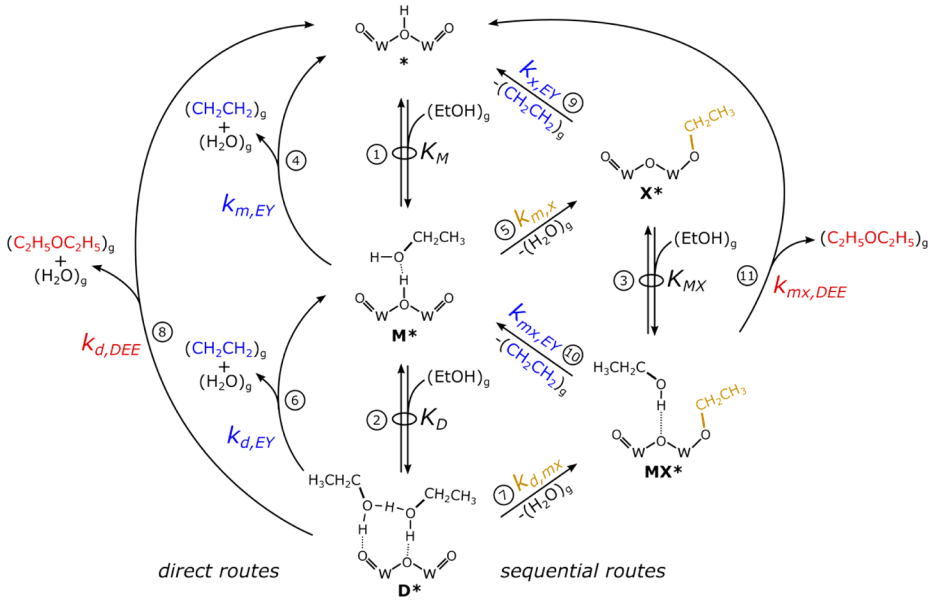

[a]Surface intermediate labels correspond to bare protons (*), EtOH monomers (M*), protonated EtOH dimers (D*), ethoxides (X*), and ethoxide/EtOH site pairs (MX*). Label colors indicate elementary steps that form DEE (red), EY (blue), and ethoxides (gold).

of DEE and EY formation ($r_{total} = r_{DEE} + r_{EY}$). Titration with DTBP led to dehydration rates that decreased with increasing DTBP uptakes and were fully suppressed after all protons were titrated (Figure 1; (a) H_3PW/SiO_2 and (b) H_4SiW/SiO_2). These data indicate that Brønsted acid sites account for all DEE and EY products formed and that DTBP titrates all protons in POM/SiO_2 catalysts. DTBP uptakes (per POM; Table 1) are smaller than stoichiometric values (i.e., $8 - x$ where x is the valence of the central atom) for all POM catalysts, suggesting that some protons are inaccessible to EtOH and DTBP or are not present at reaction conditions; this may reflect intracluster or intercluster POM dehydroxylations, which remove some H^+ and POM O atoms as H_2O, or condensation reactions of OH groups in POM clusters with support silanols.[51−53] Total dehydration turnover rates for each sample are reported here normalized by the number of H^+ titrated by DTBP during catalysis.

Figure 2a shows measured total dehydration turnover rates (per accessible H^+) as a function of EtOH pressure on each POM/SiO_2 catalyst. Turnover rates are initially proportional to EtOH pressure but become insensitive to EtOH at higher pressures, a transition that occurs at higher pressures for POM clusters with lower-valent central atoms. The areal density of protons (0.09−0.18 H^+ (nm^2 SiO_2)$^{-1}$) did not influence turnover rates on H_3PW/SiO_2 catalysts (Figure 2a), suggesting that measured rates are unaffected by intraparticle ethanol concentration gradients, which would become stronger with increasing H^+ density. The lower reactivity of POM clusters

DOI: 10.1021/acs.jpcc.5b11127
J. Phys. Chem. C 2016, 120, 3371−3389

with central atoms other than P on the same silica support precludes any effect of transport corruptions on these other catalysts.

The ratios of DEE formation to EY formation rates (r_{DEE}/r_{EY}) are shown in Figure 2b as a function of EtOH pressure on all H_nXW/SiO_2 samples. These rate ratios increase sharply with increasing EtOH pressure at first and then more gradually at higher pressures; their values were similar for H_nXW/SiO_2 samples with different central atoms and did not depend on areal H^+ density (Figure 2b), indicating that selectivities are unaffected by diffusion-enhanced interconversions of EY and DEE products within acid domains. Consequently, the nonlinear relationship between EtOH pressure and r_{DEE}/r_{EY} in Figure 2b, and the nonzero EY formation rates at high EtOH pressures of practical applications, are kinetic in origin.

3.1. Mechanism for EY and DEE Formation. Conventional mechanisms that propose only monomolecular elementary steps for EY formation and bimolecular steps for DEE formation predict a simple linear relation between EtOH pressure and r_{DEE}/r_{EY} with a zero intercept

$$\frac{r_{DEE}}{r_{EY}} = \frac{k_{DEE}[EtOH]}{k_{EY}} \tag{5}$$

in sharp contrast with the data in Figure 2b. Therefore, the elementary steps that actually contribute to EY and DEE formation must include at least two distinct pathways (with different EtOH pressure effects) to form one or both dehydration products. In what follows, we assemble a comprehensive set of plausible elementary steps for EY and DEE formation (Scheme 1) and evaluate their kinetic relevance using systematic protocols based on sensitivity and rate-of-production analyses together with thermodynamic and kinetic constants derived from density functional theory.

These plausible EtOH dehydration catalytic sequences (Scheme 1) include direct and sequential (alkoxide-mediated) routes (Steps 1−5, 8, 9, 11). These steps account for EY and DEE formation from ethanol[3,5,11,12,54−58] and for the direct formation of EY from protonated EtOH dimers (Step 6), also proposed in the case of butanol dehydration on MFI zeolites;[59] additional steps, first proposed herein, account for bimolecular ethoxide formation and EtOH-assisted ethoxide deprotonation (Steps 7 and 10, respectively). The mechanism depicted in Scheme 1 involves five surface intermediates (bare protons (*), EtOH monomers (M*), protonated EtOH dimers (D*), ethoxides (X*), and ethoxide/EtOH site pairs (MX*)), three quasi-equilibrated steps (Steps 1−3), and eight irreversible steps (Steps 4−11). The reverse reactions for Steps 4−11 all depend on the concentrations of one or more dehydration products (EY, DEE, or H_2O). The irreversibility of these steps is evident from total dehydration rates and product formation rate ratios that do not depend on space velocity and, consequently, on the concentrations of dehydration products on H_4SiW/SiO_2 at differential EtOH conversions (Figure S1−1 in Supporting Information (SI)), indicating that Steps 4−11 do not proceed at detectable rates in their reverse direction at the conditions of our experiments.

In these pathways, EtOH physisorbs at unoccupied Brønsted acid sites (Step 1; quasi-equilibrated) by forming an H-bond between the O atom in EtOH and a proton. This H-bonded EtOH (or EtOH monomer) then protonates and reorients to eliminate H_2O to form a π-bonded EY that desorbs without protonation (Step 4) or an ethoxide at a terminal O atom (Step 5). This ethoxide can form EY directly by cleaving its covalent C−O bond, leaving the H^+ at a bridging O atom (Step 9). The adsorption of another EtOH at an O atom adjacent to an EtOH monomer (Step 2; quasi-equilibrated) leads to the full transfer of the proton to the EtOH monomer to form protonated EtOH dimers, which can rearrange and release H_2O to form a protonated DEE that deprotonates and desorbs (Step 8); these dimers can also form a π-bonded EY adjacent to an adsorbed EtOH (from which EY desorbs; Step 6) or an ethoxide bound to a terminal O atom with an adjacent EtOH (Step 7). EtOH adsorption next to an ethoxide (Step 3, quasi-equilibrated) forms a weak H-bond between the OH in EtOH and a bridging O atom on the POM acid. The coadsorbed EtOH molecule can react with the bound ethoxide by either a substitution reaction, in which the EtOH O atom forms a bond with the α-carbon atom of the ethoxide while displacing the POM terminal O atom to form DEE (Step 11), or acting as a proton shuttle in assisting EY formation (Step 10).

The elementary steps depicted in Scheme 1 taken together with the assumptions of quasi-equilibrated EtOH physisorption at H^+ and at O atoms vicinal to ethoxides or EtOH monomers (Steps 1−3), of irreversible elimination and substitution steps (Steps 4−11), and of pseudo-steady-state for all bound species give equations for the rates of EY formation

$$\frac{r_{EY}}{[H^+]} = \{[k_{m,EY} + k_{d,EY}K_D[EtOH] + (k_{m,x} + k_{d,mx}K_D[EtOH])(1 - f_{x\to DEE})]K_M[EtOH]\} / \{1 + (1 + \beta)K_M[EtOH] + (K_D + \beta K_{MX}) K_M[EtOH]^2\} \tag{6}$$

and DEE formation

$$\frac{r_{DEE}}{[H^+]} = \{[k_{d,DEE}K_D[EtOH] + (k_{m,x} + k_{d,mx}K_D[EtOH]) f_{x\to DEE}]K_M[EtOH]\} / \{1 + (1 + \beta)K_M[EtOH] + (K_D + \beta K_{MX})K_M[EtOH]^2\} \tag{7}$$

In these equations, $f_{x\to DEE}$ is given by

$$f_{x\to DEE} = \frac{k_{mx,DEE}K_{MX}[EtOH]}{k_{x,EY} + (k_{mx,EY} + k_{mx,DEE})K_{MX}[EtOH]} \tag{8}$$

and represents the fraction of the ethoxide consumed that forms DEE. The β term, in turn, is given by

$$\beta = \frac{k_{m,x} + k_{d,mx}K_D[EtOH]}{k_{x,EY} + (k_{mx,EY} + k_{mx,DEE})K_{MX}[EtOH]} \tag{9}$$

and reflects the ratio of ethoxide to EtOH monomer at surfaces. The rate constants are: (i) $k_{m,EY}$ and $k_{m,x}$ for H_2O elimination from monomers for EY (Step 4) and for ethoxide formation (Step 5); (ii) $k_{d,DEE}$, $k_{d,EY}$, and $k_{d,mx}$ for H_2O elimination from EtOH dimers to form DEE (Step 8), EY (Step 6), and ethoxide (Step 7); (iii) $k_{x,EY}$ and $k_{mx,EY}$ for EY formation from ethoxides via unassisted (Step 9) and EtOH-assisted (Step 10) routes; and (iv) $k_{mx,DEE}$ for DEE formation from ethoxides (Step 11). The K_M, K_D, and K_{MX} parameters denote, respectively, the equilibrium constants for EtOH physisorption at protons (Step 1) and at O atoms vicinal to EtOH monomers (Step 2) or ethoxides (Step 3). $[H^+]$ represents the total number of

DOI: 10.1021/acs.jpcc.5b11127
J. Phys. Chem. C 2016, 120, 3371−3389

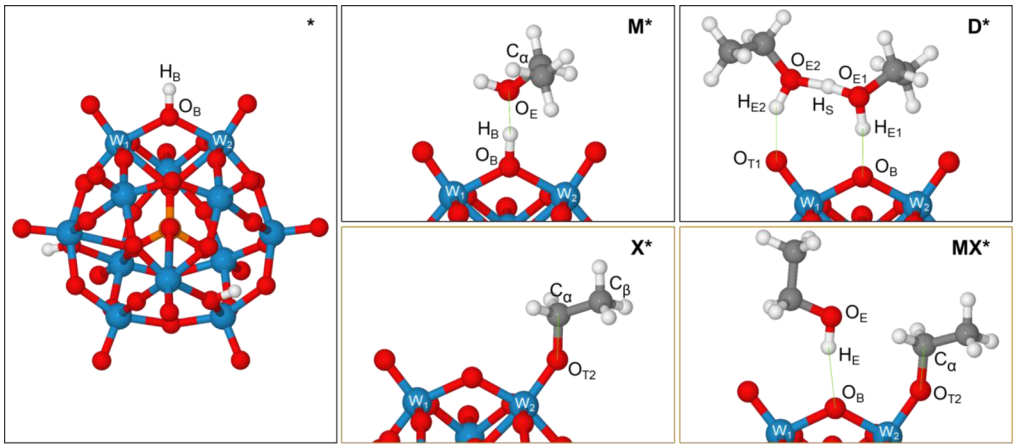

Figure 3. Structures for surface intermediates in Scheme 1 on $H_3PW_{12}O_{40}$: bare protons (*), EtOH monomers (M*), protonated EtOH dimers (D*), ethoxides (X*), and ethoxide/EtOH site pairs (MX*).

protons, determined by titration with 2,6-di-*tert*-butylpyridine during EtOH dehydration (Table 1).

In Section 3.2, DFT-derived free energies for intermediates and transition states are used together with sensitivity analysis protocols to determine the magnitude of the rate and equilibrium constants in eqs 6−9 and the respective contributions of each of the routes in Scheme 1 to the observed rates of formation of EY and DEE.

3.2. Theoretical Treatments of Intermediates and Transition States in Ethanol Dehydration on POM Clusters. *3.2.1. EtOH Adsorption at Protons and at O Atoms Vicinal to EtOH Monomers and Ethoxides.* EtOH interacts with protons attached to O atoms in POM clusters (Step 1 in Scheme 1) to form a strong bond between the POM proton (H_B; nomenclature defined in Figure 3) and the O atom in EtOH (O_E) (M*; Figure 3); the O_B−O_E distance in M* (2.50−2.55 Å; Table 2) is much shorter than in H-bonded alkanols (2.74 Å),[36,60,61] suggesting that the POM proton is partially transferred to the EtOH molecule. The O_B−H_B bond in M* resembles that in the bare POM cluster (O_B−H_B = 0.97 Å vs 1.04−1.06 Å for M*; Table 2) and is much shorter than the bond between the O atom in EtOH and H_B (O_E−H_B = 1.44−1.51 Å for M*; Table 2), indicating that adsorbed EtOH monomers are not fully protonated by POM clusters because proton transfer would result in longer O_B−H_B and shorter O_E−H_B bonds than in M*. Yet, the charge on the H_B atom decreases from 0.443−0.452 in the bare proton to 0.376−0.379 in M* (Table 2), and the POM conjugate anion becomes more negatively charged (0.443−0.452 in *; 0.539−0.568 in M*) with the additional net positive charge residing at the adsorbed EtOH (0.160−0.192 in M*), consistent with significant electronic reorganization upon formation of the H-bond. EtOH adsorption enthalpies were more negative on POM clusters with smaller DPE values (stronger acids; Figure 4a), ranging from −75.5 kJ mol^{-1} on the weakest acid ($H_6CoW_{12}O_{40}$, DPE = 1141 kJ mol^{-1}) to −86.7 kJ mol^{-1} on the strongest acid ($H_3PW_{12}O_{40}$, DPE = 1085 kJ mol^{-1}); these trends are consistent with the higher energetic cost of charge separation and the lower stability of the negative charge at the conjugate base for the weaker acids. EtOH adsorption enthalpies vary by less than concomitant changes in DPE (ΔH_{ads} = 11.2 kJ mol^{-1} vs ΔDPE = 56 kJ mol^{-1} going from $H_3PW_{12}O_{40}$ to $H_6CoW_{12}O_{40}$) because negative charges on POM anions decrease (0.568−0.539 for M*) as acids weaken, thus attenuating the greater energetic costs of charge separation in weaker acids. These adsorption enthalpies indicate that the interactions between EtOH and POM protons are much stronger than for H-bonding among gaseous EtOH molecules (−21 kJ mol^{-1} per H-bond),[62] as a consequence of electrostatic interactions between the partially charged H_B and the O atom in EtOH. EtOH adsorption entropies are negative (Figure 4b) because EtOH(g) loses significant mobility upon adsorption. These entropy losses are smaller on weaker acids because the O_B−H_B distances (Table 2) and the partial charges in adsorbed EtOH (Table 2) are smaller than on stronger acids to offset the higher costs of charge separation on weaker acids; as a result, the H_B−O_E bond is weaker and the adsorbed EtOH less rigid.

A second EtOH molecule can adsorb at an O atom adjacent to the EtOH monomer (Step 2 in Scheme 1) to form additional H-bonds with the O atom and the coadsorbed EtOH. The most stable structure of these EtOH dimers (D* in Figure 3) contains an O_{E1}−H_S−O_{E2} bridge between the two EtOH molecules, as well as a H-bond between each EtOH and a POM O atom. The O−O distances between the two EtOH molecules (O_{E1}−O_{E2} = 2.44−2.46 Å; Table 2) are shorter than for O_{E1}−O_B and O_{E2}−O_{T1} bonds between EtOH and the surface (2.50−2.60 Å and 2.60−2.66 Å, respectively; Table 2). These dimers (EtOH−H_S−EtOH) are more cationic than EtOH monomers (0.701−0.776 for D* vs 0.539−0.568 for M*, range for POM clusters with different central atoms; Table 2), consistent with the more complete transfer of the proton upon dimer formation. The dimer formation enthalpies (from EtOH monomers and EtOH(g)) are large and negative (−74.1 to −85.9 kJ mol^{-1}; Figure 4a) and become less negative with increasing DPE (Figure 4a) because the concomitant increase in energetic costs of charge separation is offset only in part by their smaller charge in the conjugate anion (0.776−0.701 for D*). Dimer formation entropies are negative (Figure 4b) as a result of the binding of the second EtOH molecule, and more so than for EtOH monomer formation (Figure 4b) because the O_{E1}−H_S−O_{E2} bridge in dimers (Figure 3) makes the bound EtOH molecules more rigid. Entropy losses are larger on weaker acids, consistent with their shorter O_B−H_{E1} and O_{T1}−H_{E2} bonds (Table 2), which compensate for the higher cost of charge separation in weaker acids by decreasing the amount and the separation of charges, thus making dimers slightly more rigid on weaker acids.

DOI: 10.1021/acs.jpcc.5b11127
J. Phys. Chem. C 2016, 120, 3371−3389

Table 2. Atomic Distances (Å), Bond and Dihedral Angles (degrees), and Charges (Electron Charges) Of Surface Intermediates on Keggin POM Clusters

species[a]	central atom			
	P	Si	Al	Co
bare cluster (*)				
O_B–H_B	0.97	0.97	0.97	0.97
charge – H_B	0.452	0.451	0.449	0.443
EtOH monomer (M)*				
O_B–O_E	2.50	2.52	2.53	2.55
O_B–H_B	1.06	1.05	1.05	1.04
O_E–H_B	1.44	1.48	1.48	1.51
C_α–O_E	1.47	1.46	1.46	1.46
charge – H_B	0.376	0.379	0.379	0.379
charge – EtOH	0.192	0.176	0.173	0.160
charge – EtOH + H_B	0.568	0.555	0.552	0.539
protonated EtOH dimer (D)*				
O_{E1}–O_{E2}	2.45	2.45	2.44	2.46
O_{E1}–H_S	1.11	1.10	1.10	1.08
O_{E2}–H_S	1.35	1.36	1.35	1.39
O_{E1}–O_B	2.60	2.57	2.56	2.50
O_{E1}–H_{E1}	1.03	1.04	1.04	1.07
O_B–H_{E1}	1.58	1.53	1.53	1.44
O_{E2}–O_{T1}	2.66	2.63	2.60	2.60
O_{E2}–H_{E2}	1.00	1.00	1.00	1.00
O_{T1}–H_{E2}	1.74	1.71	1.67	1.66
$\angle O_B$–H_{E1}–O_{E1}	172.3°	171.4°	168.7°	169.3°
$\angle O_{E1}$–H_S–O_{E2}	171.9°	171.8°	171.5°	171.5°
$\angle O_{E2}$–H_{E2}–O_{T1}	151.6°	151.8°	153.8°	154.4°
charge – EtOH dimer	0.776	0.754	0.741	0.701
ethoxide (X)*				
O_{T2}–C_α	1.45	1.44	1.44	1.43
C_α–C_β	1.51	1.51	1.51	1.51
H_β–C_β	1.10	1.10	1.10	1.10
$\angle W_2$–O_{T2}–C_α	145.0°	147.1°	147.4°	150.2°
charge – ethyl ($C_\alpha H_2 C_\beta H_3$)	0.350	0.344	0.340	0.332
ethoxide/EtOH site pair (MX)*				
O_{T2}–C_α	1.46	1.45	1.44	1.44
O_E–O_B	2.93	2.91	2.89	2.86
O_E–H_E	0.98	0.98	0.98	0.98
O_B–H_E	1.97	1.95	1.92	1.89
$\angle W_2$–O_{T2}–C_α	149.5°	154.5°	154.5°	154.8°
charge – ethyl ($C_\alpha H_2 CH_3$)	0.365	0.360	0.354	0.346
charge – EtOH	−0.013	−0.019	−0.010	−0.032
charge – ethyl + EtOH	0.352	0.341	0.344	0.314

[a]Atomic and structural labels correspond to diagrams in Figure 3.

The adsorption of an EtOH molecule at an O atom adjacent to an ethoxide (Step 3; Scheme 1) forms a bond between the H atom in the EtOH hydroxyl group and an O atom in the POM cluster (MX*; Figure 3). W_2–O_{T2}–C_α bond angles in ethoxides (X*; Figure 3) increased slightly upon EtOH coadsorption to form MX* ($\angle W_2$–O_{T2}–C_α = 149.5–154.8° for MX* vs 145.0–150.2° for X*; Figure 4, Table 2). The enthalpies of MX* formation (from X* and EtOH(g)) (−29.6 to −34.8 kJ mol^{-1}; Figure 4a) resemble those in the H-bonds prevalent among gaseous EtOH molecules (−21 kJ mol^{-1})[62] but are much less negative than that for EtOH adsorption at POM protons (−75.5 to −86.7 kJ mol^{-1}; Figure 4a) or at POM O atoms adjacent to EtOH monomers (−74.1 to −85.9 kJ mol^{-1}; Figure 4a). These weak ethoxide–EtOH interactions give rise to large O_E–O_B distances (2.86–2.93 Å; Table 2), to slightly negative charges on the EtOH group (−0.010 to −0.032; Table 2), and to smaller entropy losses upon adsorption than for EtOH adsorption on protons or adjacent to EtOH monomers (Figure 4b). The enthalpies and entropies for the formation of EtOH/ethoxide moieties become slightly more negative as DPE increases because the higher electron densities in the weaker POM acids lead to stronger interactions with the H atom at the OH group in EtOH.

In Section 3.2.4, these adsorption enthalpies and entropies (Figure 4) are used to estimate the relative abundance of these bound species, which interconvert via the quasi-equilibrated steps shown in Scheme 1 (*–M*–D*; Steps 1, 2; X*–MX*; Step 3). In contrast with quasi-equilibrium concentrations of these species, the concentration of ethoxides (X*, MX*) relative to those interacting with bare protons or EtOH(g) (M*, D*) reflect their relative rates of formation (Steps 5, 7) and consumption (Steps 9–11), as prescribed by the pseudo-steady-state hypothesis.

3.2.2. Ethylene Formation via syn-E2-Type Elimination Steps from EtOH Monomers, EtOH Dimers, Ethoxides, and EtOH/Ethoxide Pairs. All four routes leading to EY in Scheme 1 (Steps 4, 6, 9, 10) involve a concerted *syn*-E2-type elimination, in which a C_α–O_L bond cleaves with the concerted abstraction of a β-hydrogen atom by a basic O atom (O_R). When EY forms directly from EtOH monomers or dimers, this β-hydrogen (H_β) is abstracted by a POM O atom, and C_α–O_L cleavage either releases a H_2O(g) molecule (direct monomolecular EY formation; TS4; Figure 5) or forms a H_2O that interacts via H-bonding with the vicinal EtOH (direct bimolecular EY formation; TS6 in Figure 5). Sequential EY formation routes involve the prior evolution of water and the subsequent formation of an ethoxide; these steps cleave the C_α–O_L bond between the ethoxide and the terminal O atom while a β-hydrogen atom is abstracted by either a bridging O atom in the POM (sequential monomolecular EY formation; TS9 in Figure 5) or an O atom in a coadsorbed EtOH (sequential bimolecular EY formation; TS10 in Figure 5). The β-hydrogen (H_β) and the O atom at the α-carbon (O_L) in all the elimination TS structures (TS4, TS6, TS9, and TS10) are nearly *syn*-coplanar on all POM clusters; their H_β–C_β–C_α–O_L dihedral angles range from 0.4° to 13.0° (Table 3), consistent with those expected for syn eliminations (<20°).[63] In all elimination TS structures, the C_α–O_L bonds are more elongated (relative to those in ethoxides) than the C_β–H_β bonds (44–61% for C_α–O_L; 14–31% for C_β–H_β bonds; Table 3); the $C_\alpha H_2$ fragments have positive partial charges (0.271–0.350; Table 3), while the $C_\beta H_2$ fragments are slightly negative (0.071–0.126; Table 3), indicating that C_α–O_L bond cleavage is farther along the reaction coordinate for C_α–O_L bonds than C_β–H_β bonds at the TS. The simultaneous proton transfer, double bond formation, and expulsion of the leaving group at these TS is consistent with those for *syn*-E2-type eliminations.[63−65] E2-type elimination TS structures can vary from being "$E1_{cb}$-like" when C–H cleavage is more advanced than C–O cleavage, to being "E1-like" in the other extreme (when C–O cleavage is more advanced than C–H cleavage).[64] Thus, the elimination TS structures for direct and sequential routes are more precisely characterized as *syn*-E2-type TS with some "E1-like" character.

The POM conjugate anions are more negatively charged for sequential bimolecular EY formation (0.667–0.701; TS10) and

DOI: 10.1021/acs.jpcc.5b11127
J. Phys. Chem. C 2016, 120, 3371–3389

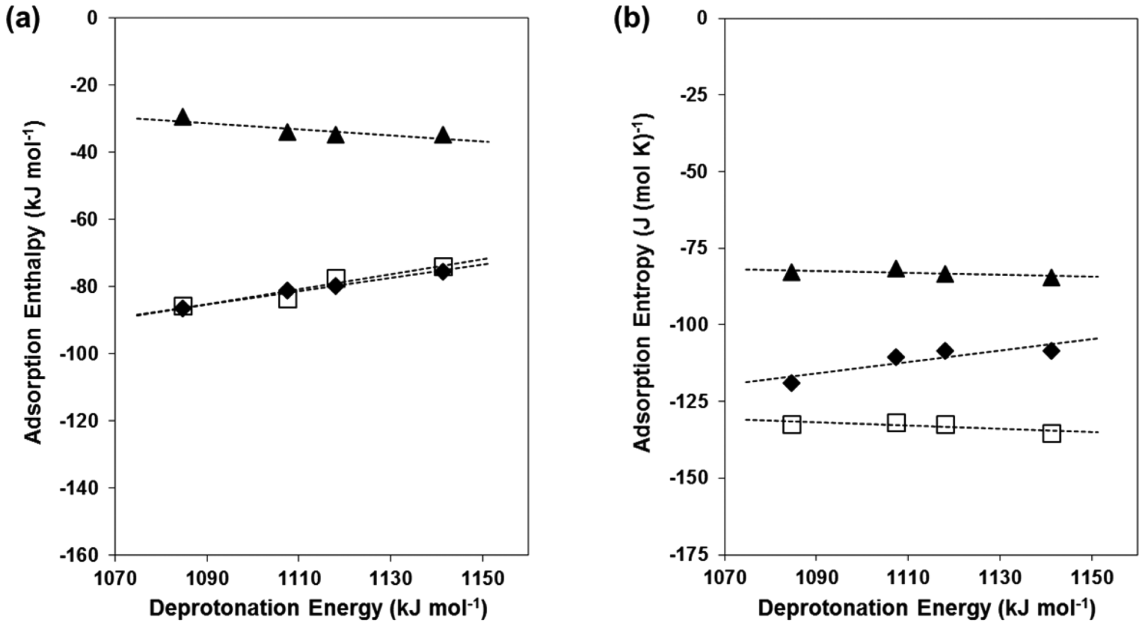

Figure 4. Calculated (a) adsorption enthalpies and (b) adsorption entropies as functions of DPE for monomers (M* in Figure 3, ◆) relative to a bare cluster and $EtOH_{(g)}$, protonated dimers (D* in Figure 3, □) relative to an EtOH monomer and $EtOH_{(g)}$, and for ethoxide/EtOH site pairs (MX* in Figure 3, ▲) relative to an ethoxide (X* in Figure 3) and $EtOH_{(g)}$ for $H_{8-n}X^{n+}W_{12}O_{40}$ (X^{n+} = P^{5+}, Si^{4+}, Al^{3+}, and Co^{2+}). Dashed lines are linear best fits of the calculated values to changes in DPE.

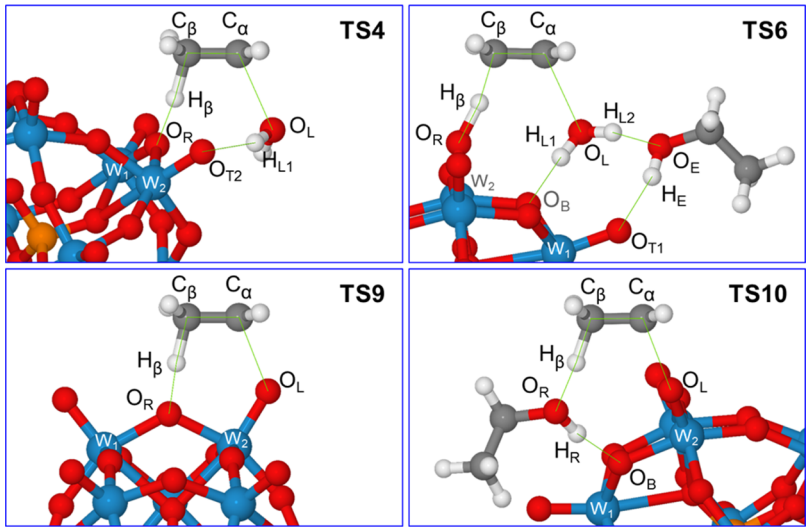

Figure 5. Structures of transition states that mediate elementary steps in Scheme 1 for direct monomolecular EY formation (Step 4; TS4), direct bimolecular EY formation (Step 6; TS6), sequential monomolecular EY formation (Step 9; TS9), and sequential bimolecular EY formation (Step 10; TS10) on $H_3PW_{12}O_{40}$.

direct monomolecular EY formation (0.607−0.668; TS4) transition states than for sequential monomolecular EY formation (0.530−0.570; TS9). This is consistent with favorable ion−dipole interactions between the additional H_2O and EtOH fragments in TS4 and TS10 and the POM O atoms, which cause the transfer of more charge from the POM conjugate anions to the cationic moieties at the TS. Weaker acids give smaller charges at the conjugate anion in TS4, TS9, and TS10 than stronger acids because the charge at the conjugate anion is less stable. Proton transfer has occurred to a much greater extent in TS6 than in TS4 or TS10 as evidenced by their shorter O_R−H_β bonds (1.22−1.30 Å; TS6, 1.32−1.44 Å; TS4 and TS10) and smaller charges on $C_\alpha H_2$ (0.275−0.289; TS6, 0.287−0.350; TS4 and TS10). Also, TS6 exhibits less negative conjugate anions (0.565−0.577; TS6) than TS4 and TS10 (0.607−0.668; TS4, 0.667−0.701; TS10), in spite of its additional EtOH or H_2O fragments, suggesting that ion−dipole interactions between the H_2O and EtOH fragments and the POM O atoms are less favorable in TS6 than in TS4 or TS10.

Figure 6a shows enthalpies for all elimination TS structures (TS4, TS6, TS9, and TS10) referenced to a bare proton and two EtOH(g) as a function of DPE for $H_{8-n}X^{n+}W_{12}O_{40}$ clusters with different central atoms (X^{n+} = P^{5+}, Si^{4+}, Al^{3+}, and Co^{2+}). These enthalpic barriers are larger for TS moieties with fewer molecular fragments (ethyl, EtOH, or H_2O). For instance, the TS for sequential monomolecular EY formation (TS9; Figure 5), with a single ethyl fragment, has the highest barriers (Figure 6a), while the TS for direct bimolecular EY formation (TS6;

DOI: 10.1021/acs.jpcc.5b11127
J. Phys. Chem. C 2016, 120, 3371−3389

Table 3. Atomic Distances (Å), Bond and Dihedral Angles (degrees), and Charges (Electron Charges) For Transition States That Mediate Ethylene Formation on Keggin POM Clusters

species[a]	central atom P	Si	Al	Co
direct monomolecular EY formation (TS4)				
O_R–H_β	1.37	1.32	1.34	1.33
C_β–H_β	1.28	1.31	1.30	1.30
C_α–C_β	1.39	1.39	1.39	1.39
C_α–O_L	2.25	2.21	2.18	2.16
H_{L1}–O_{T1}	1.89	1.76	1.75	1.71
$\angle H_\beta$–C_β–C_α–O_L	12.0°	2.8°	1.8°	0.4°
charge – ethyl ($C_\alpha H_2 C_\beta H_2 H_\beta$)	0.550	0.512	0.506	0.486
charge – H_β	0.299	0.304	0.302	0.300
charge – $C_\beta H_2$	−0.075	−0.092	−0.096	−0.101
charge – $C_\alpha H_2$	0.326	0.300	0.299	0.287
charge – leaving H_2O group	0.118	0.116	0.121	0.121
charge – cationic moiety	0.668	0.628	0.627	0.607
direct bimolecular EY formation (TS6)				
O_R–H_β	1.22	1.22	1.26	1.30
C_β–H_β	1.39	1.40	1.35	1.33
C_α–C_β	1.38	1.38	1.38	1.39
C_α–O_L	2.32	2.30	2.28	2.29
H_{L1}–O_B	1.90	1.87	1.85	1.83
H_{L2}–O_E	1.73	1.72	1.76	1.76
H_E–O_{T1}	1.86	1.85	1.87	1.85
$\angle H_\beta$–C_β–C_α–O_L	5.4°	7.9°	9.8°	12.3°
charge – ethyl ($C_\alpha H_2 C_\beta H_2 H_\beta$)	0.519	0.506	0.512	0.504
charge – H_β	0.340	0.339	0.332	0.327
charge – $C_\beta H_2$	−0.096	−0.103	−0.105	−0.112
charge – $C_\alpha H_2$	0.275	0.271	0.285	0.289
charge – H_2O leaving group	0.018	0.021	0.031	0.039
charge – EtOH	0.039	0.038	0.034	0.032
charge–cationic moiety	0.576	0.565	0.577	0.575
sequential monomolecular EY formation (TS9)				
O_R–H_β	1.40	1.37	1.37	1.38
C_β–H_β	1.26	1.27	1.27	1.25
C_α–C_β	1.40	1.40	1.40	1.40
C_α–O_L	2.14	2.12	2.10	2.08
$\angle H_\beta$–C_β–C_α–O_L	4.4°	3.2°	3.1°	3.2°
charge – ethyl ($C_\alpha H_2 C_\beta H_2 H_\beta$)	0.570	0.549	0.540	0.530
charge – H_β	0.292	0.295	0.297	0.295
charge – $C_\beta H_2$	−0.071	−0.079	−0.086	−0.098
charge – $C_\alpha H_2$	0.349	0.333	0.329	0.334
charge – cationic moiety	0.570	0.549	0.540	0.530
sequential bimolecular EY formation (TS10)				
O_R–H_β	1.44	1.42	1.43	1.39
H_β–C_β	1.25	1.26	1.26	1.28
C_α–C_β	1.40	1.40	1.40	1.40
C_α–O_L	2.07	2.05	2.09	2.08
H_R–O_B	1.72	1.67	1.65	1.60
$\angle H_\beta$–C_β–C_α–O_L	0.5°	4.7°	13.0°	12.1°
charge – ethyl ($C_\alpha H_2 C_\beta H_2 H_\beta$)	0.524	0.507	0.515	0.494
charge – H_β	0.290	0.289	0.290	0.293
charge – $C_\beta H_2$	−0.116	−0.122	−0.115	−0.126
charge – $C_\alpha H_2$	0.350	0.340	0.340	0.327
charge – EtOH	0.177	0.180	0.174	0.173
charge – cationic moiety	0.701	0.686	0.688	0.667

[a]Atomic and structural labels correspond to diagrams in Figure 5.

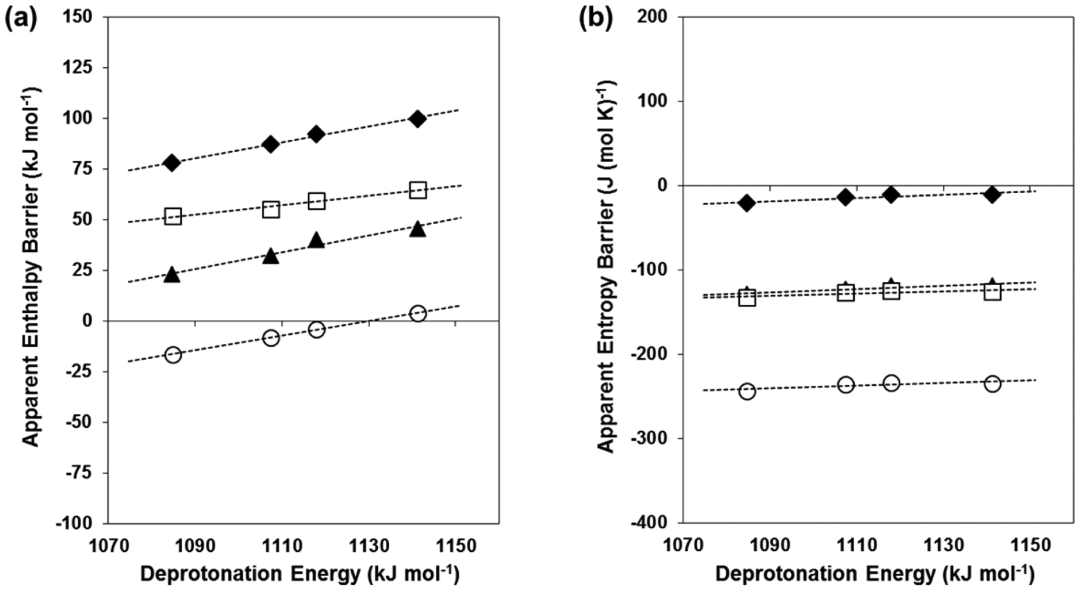

Figure 6. Calculated (a) apparent enthalpy barriers and (b) apparent entropy barriers as functions of DPE for direct monomolecular EY formation (TS4 in Figure 5, □), direct bimolecular EY formation (TS6 in Figure 5, ○), sequential monomolecular EY formation (TS9 in Figure 5, ◆) and sequential bimolecular EY formation (TS10 in Figure 5, ▲) on $H_{8-n}X^{n+}W_{12}O_{40}$ (X^{n+} = P^{5+}, Si^{4+}, Al^{3+}, and Co^{2+}). Barriers are with respect to bare protons and two EtOH(g) molecules.

DOI: 10.1021/acs.jpcc.5b11127
J. Phys. Chem. C 2016, 120, 3371−3389

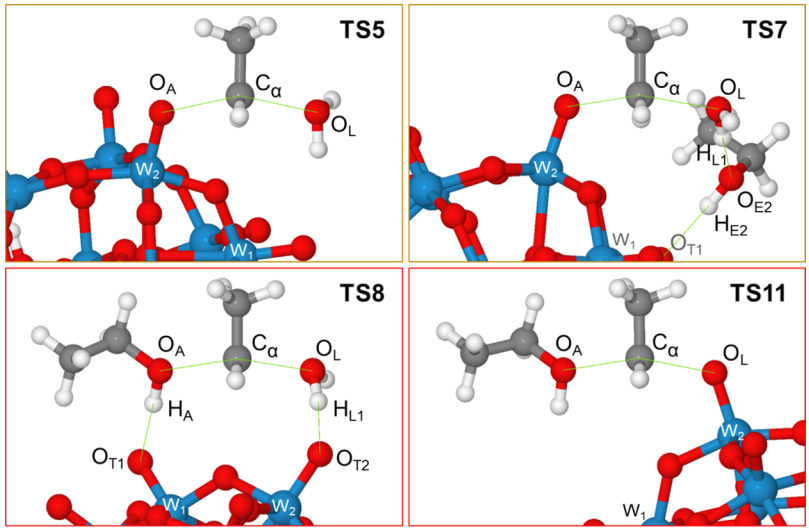

Figure 7. Structures of transition states that mediate elementary steps in Scheme 1 for monomolecular ethoxide formation (Step 5, TS5), bimolecular ethoxide formation (Step 7, TS7), direct DEE formation (Step 8, TS8), and sequential DEE formation (Step 11, TS11) on $H_3PW_{12}O_{40}$.

Figure 5), with ethyl, EtOH, and H_2O fragments, shows the lowest barriers (Figure 6a) among elementary steps that lead to EY on all POM acids. These trends reflect the larger number of H-bonds and ion−dipole interactions at TS structures containing additional EtOH or H_2O molecules. This enthalpic stabilization, conferred by the presence of several fragments (Figure 9), is attenuated by concomitant entropy losses upon formation of the larger and more complex TS structures (Figure 6b). Weaker acids (larger DPE values) give larger enthalpy barriers for all EY formation routes than stronger acids (Figure 6a) because the formation of all TS structures requires charge transfer into the POM clusters to form the cationic organic moiety at the TS (0.530−0.701; Table 3). The enthalpy and entropy barriers in Figure 4 are used in Section 3.2.4, together with those for the formation of DEE and alkoxides (Section 3.2.3) to determine the relative contributions of these elimination steps (Steps 4, 6, 9, and 10) to EY formation.

3.2.3. DEE and Ethoxide Formation via SN2-Type Pathways. All steps that form ethoxides (Steps 5 and 7; Figure 3) or DEE (Steps 8 and 11; Figure 3) involve S_N2-type reactions that cleave and form O−C bonds at the α-carbon (C_α) of an ethyl fragment in a concerted manner (Figure 7). In ethoxide formation, a terminal POM O atom acts as the nucleophile in displacing either a H_2O molecule (monomolecular ethoxide formation; TS5 in Figure 7) or a H_2O molecule that is H-bonded to a coadsorbed EtOH (bimolecular ethoxide formation; TS7 in Figure 7) at the C_α of a protonated EtOH monomer, thus forming the new O−C_α bond. In DEE formation, the O atom in a coadsorbed EtOH acts as the nucleophile in displacing either a H_2O molecule at the C_α of a protonated EtOH (direct DEE formation; TS8 in Figure 7) or a terminal POM O atom (sequential DEE formation; TS11 in Figure 7) at the C_α of an ethoxide, thus forming the new O−C_α bond. The C_α atom in the ethyl cationic species ($C_\alpha H_2CH_3$) at the TS structures for all S_N2-type substitution steps is nearly equidistant from the attacking (O_A) and leaving (O_L) O atoms (C_α−O_A = 1.99−2.20 Å; C_α−O_L = 2.04−2.15 Å; Table 4); this C_α center is pentacoordinated with a nearly trigonal bipyramidal geometry, consistent with the concerted nature and the required orbital alignment of S_N2-type substitution reactions. Also, the partial charges in $C_\alpha H_2CH_3$ fragments at the TS (0.484−0.553; Table 4) are smaller than unity, consistent with solvation of the sp^2-hybridized α-carbon and with the concomitant delocalization of its positive charge by the attacking and leaving groups.

Figure 8a shows the enthalpies of these S_N2-type transition states (referenced to a bare POM proton and two EtOH(g)) as a function of DPE for $H_{8-n}X^{n+}W_{12}O_{40}$ clusters (X^{n+} = P^{5+}, Si^{4+}, Al^{3+}, and Co^{2+}). The enthalpy barriers for bimolecular ethoxide formation (TS7; Figure 7) and direct DEE formation (TS8; Figure 7) are similar to each other on each given POM acid and smaller than those for monomolecular ethoxide formation (TS5; Figure 7) or sequential DEE formation (TS11; Figure 7) (by 64.9−73.4 and 94.5−103.5 kJ mol^{-1}, respectively), consistent with their larger number of H-bonds and ion−dipole interactions. Enthalpy barriers for all of the S_N2-type TS structures were smaller on the stronger POM acids because of the more stable conjugate anions at these transition states. Entropy losses upon formation of S_N2-type transition states (Figure 8b) are larger for transition states with additional molecular fragments (TS7 and TS8), consistent with the decrease in entropy accompanying the adsorption of EtOH(g) (Figure 4b).

In the next section, sensitivity and coverage analysis protocols are used to assess how each transition state (and its associated precursor steps) and surface intermediate contribute to EY and DEE formation on these solid Brønsted acids. These assessments are based on the DFT-derived enthalpies and entropies shown in Figures 4, 6, and 8 (values also shown in Tables S2−1 and S2−2 in SI).

3.2.4. Gibbs Free Energy Comparisons Among TS and Surface Intermediates in Ethylene and Diethyl Ether Formation Routes. Figure 9 shows Gibbs free energies at 409 K for all transition states and surface intermediates in Scheme 1 referenced to a common precursor state (a bare proton and two EtOH(g)) on the strongest ($H_3PW_{12}O_{40}$; solid lines) and the weakest ($H_6CoW_{12}O_{40}$; dashed lines) acids. $H_6CoW_{12}O_{40}$ gives higher Gibbs free energy barriers for all TS structures than $H_3PW_{12}O_{40}$. The direct monomolecular EY formation route (TS4; Figure 5) shows free energy barriers similar to those for the monomolecular ethoxide formation route (TS5; Figure 7) on $H_3PW_{12}O_{40}$. On $H_6CoW_{12}O_{40}$,

DOI: 10.1021/acs.jpcc.5b11127
J. Phys. Chem. C 2016, 120, 3371−3389

Table 4. Atomic Distances (Å), Bond and Dihedral Angles (degrees), and Charges (Electron Charges) For Transition States That Mediate Ethoxide and Diethyl Ether Formation on Keggin POM Clusters

species[a]	central atom			
	P	Si	Al	Co
monomolecular ethoxide formation (TS5)				
O_A–C_α	2.16	2.17	2.17	2.20
C_α–O_L	2.12	2.11	2.08	2.08
$\angle O_A$–C_α–O_L	155.7°	152.9°	153.2°	146.9°
charge – ethyl ($C_\alpha H_2CH_3$)	0.553	0.551	0.540	0.545
charge – H_2O leaving group	0.205	0.207	0.222	0.218
charge – cationic moiety	0.759	0.758	0.762	0.762
bimolecular ethoxide formation (TS7)				
O_A–C_α	1.99	2.00	2.01	2.02
C_α–O_L	2.15	2.13	2.15	2.15
H_{L1}–O_{E2}	1.62	1.59	1.61	1.62
H_{E2}–O_{T1}	1.99	1.92	1.86	1.90
$\angle O_A$–C_α–O_L	161.4°	161.8°	159.7°	159.1°
charge – ethyl ($C_\alpha H_2CH_3$)	0.504	0.494	0.494	0.486
charge – H_2O leaving group	0.091	0.091	0.093	0.092
charge – EtOH	0.086	0.084	0.074	0.075
charge – cationic moiety	0.680	0.669	0.661	0.653
direct DEE formation (TS8)				
O_A–C_α	2.12	2.12	2.11	2.09
C_α–O_L	2.06	2.06	2.06	2.04
H_A–O_{E2}	1.75	1.73	1.72	1.71
H_{L1}–O_{T2}	1.67	1.67	1.67	1.65
$\angle O_A$–C_α–O_L	161.3°	161.1°	160.9°	161.2°
charge – ethyl ($C_\alpha H_2CH_3$)	0.497	0.496	0.496	0.484
charge – H_2O leaving group	0.157	0.157	0.150	0.154
charge – EtOH	0.155	0.150	0.151	0.148
charge – cationic moiety	0.808	0.802	0.797	0.786
sequential DEE formation (TS11)				
O_A–C_α	2.10	2.07	2.13	2.09
C_α–O_L	2.06	2.08	2.09	2.10
$\angle O_A$–C_α–O_L	159.2°	153.0°	151.2°	150.8°
charge – ethyl ($C_\alpha H_2CH_3$)	0.522	0.523	0.525	0.518
charge – EtOH	0.227	0.229	0.219	0.229
charge–cationic moiety	0.750	0.753	0.744	0.747

[a]Atomic and structural labels correspond to diagrams in Figure 7.

however, free energy barriers for TS4 are lower than those for TS5. On each acid catalyst, free energy barriers for bimolecular ethoxide formation (TS7; Figure 7) and direct DEE formation (TS8; Figure 7) routes are similar to each other and lower than those for direct bimolecular EY formation (TS6; Figure 5) and monomolecular routes for direct EY or ethoxide formation. The stability of alkoxides (X*; Figure 3) is similar on $H_3PW_{12}O_{40}$ (−32.1 kJ mol^{-1}; Figure 9) and $H_6CoW_{12}O_{40}$ (−34.0 kJ mol^{-1}; Figure 9), consistent with the small charges in such alkoxide species (0.332–0.350; Table 2) and with their largely covalent attachment to terminal O atoms. Free energy barriers for sequential bimolecular EY formation (TS10; Figure 5) and sequential DEE formation (TS11; Figure 7) were similar on each given catalyst and smaller than those for sequential monomolecular EY formation routes (TS9; Figure 5).

Gibbs free energy differences among the intermediates in Figure 9 reflect their relative concentrations at equilibrium and 1 bar EtOH or H_2O gaseous species

$$RT \ln\left(\frac{[B]_{eq}}{[A]_{eq}}(P_{EtOH})^{\lambda}(P_{H_2O})^{\gamma}\right) = G_A - G_B - \lambda \cdot G_{EtOH(g)} - \gamma \cdot G_{H_2O(g)} \quad (10)$$

where $[A]_{eq}$ and $[B]_{eq}$ are the surface concentrations of any two intermediates at equilibrium; G_A and G_B are the free energies of the respective intermediates relative to bare protons and two gaseous EtOH molecules; P_{EtOH} and P_{H_2O} are in units of bars; λ and γ are the differences in the number of EtOH(g) and H_2O(g) in the A and B intermediates; and G_{EtOH} and G_{H2O} are the respective free energies of EtOH(g) and H_2O(g) molecules. The relative surface concentrations of A and B will depend on P_{EtOH} and P_{H_2O} as prescribed by eq 10 at equilibrium; away from equilibrium, their free energies cannot be compared directly to assess their relative coverages. The concentration of ethoxides (X*, MX*) relative to those intermediates interacting with bare protons or EtOH(g) (M*, D*) reflects their relative rates of formation (Steps 5 and 7) and consumption (Steps 9–11), according to the pseudo-steady-state hypothesis (not equilibrium); therefore the relative concentrations of these groups are not given by eq 10. In Section 3.2.5, the fractional coverage of each of the intermediates in Scheme 1 is determined explicitly at all relevant reaction conditions in order to rigorously assess its abundance during EtOH dehydration on these catalysts, thus avoiding the problems associated with direct free energy comparisons.

Gibbs free energy differences among the TS structures in Figure 9 give the relative rates of their associated elementary steps at equilibrium concentrations of their reactive intermediates

$$RT \ln\left(\frac{r_i}{r_j}(P_{EtOH})^{\lambda}(P_{H_2O})^{\gamma}\right) = G_j^{\ddagger} - G_i^{\ddagger} - \lambda \cdot G_{EtOH(g)} - \gamma \cdot G_{H_2O(g)} \quad (11)$$

where r_i and r_j are the turnover rates for the two elementary steps; $G_i^{\ddagger}$ and $G_j^{\ddagger}$ are the free energies of their respective transition states (relative to a bare proton and two EtOH(g)); and λ and γ are the differences in the number of EtOH(g) and H_2O(g) between their two transition states. If the reactive intermediates for two elementary steps are not at equilibrium, eq 11 cannot be used to determine their relative rates. According to Scheme 1, ethoxides (X*, MX*) are not in equilibrium with those intermediates interacting with bare protons or EtOH(g) (M*, D*); therefore, the relative contributions of the elementary steps in Scheme 1 to EtOH dehydration rates on these catalysts cannot be determined solely from direct comparisons of free energies. Rate sensitivity protocols overcome these limitations and provide a more complete theoretical framework suitable for quantitative comparisons among elementary steps. These are used next to assess the relative contributions of the elementary steps in Scheme 1 to EY and DEE formation rates.

3.2.5. Rate Sensitivity and Coverage Analyses. The previous sections have enumerated plausible sequences of

DOI: 10.1021/acs.jpcc.5b11127
J. Phys. Chem. C 2016, 120, 3371−3389

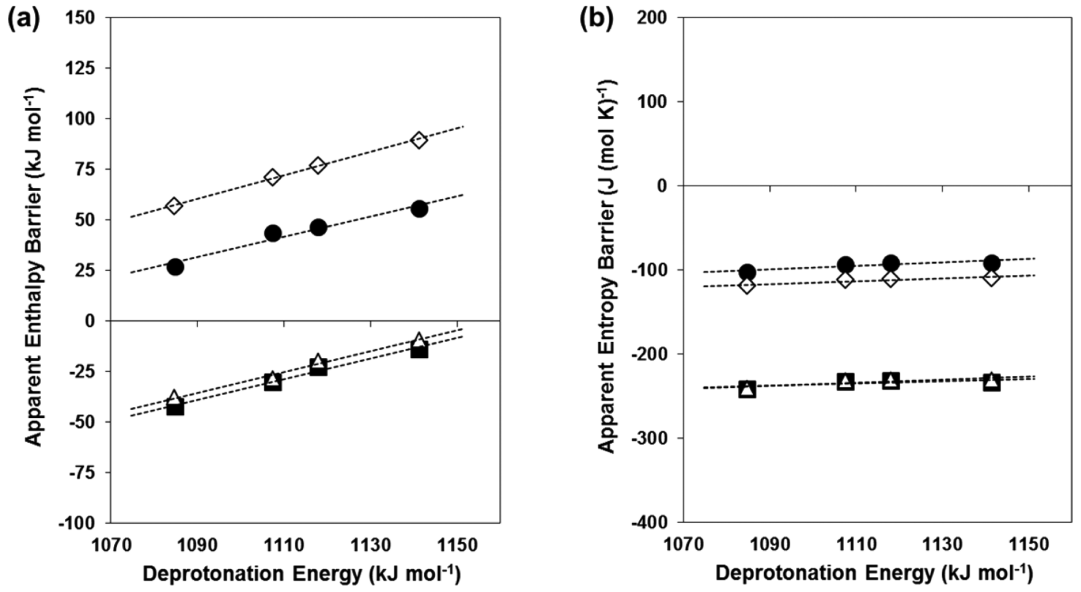

Figure 8. Calculated (a) apparent enthalpy barriers and (b) apparent entropy barriers as functions of DPE for monomolecular ethoxide formation (TS5 in Figure 7, ◇), bimolecular ethoxide formation (TS7 in Figure 7, △), direct DEE formation (TS8 in Figure 7, ■), and sequential DEE formation (TS11 in Figure 7, ●) on $H_{8-n}X^{n+}W_{12}O_{40}$ (X^{n+} = P^{5+}, Si^{4+}, Al^{3+}, and Co^{2+}). Barriers are with respect to bare clusters and two EtOH(g) molecules. Dashed lines are linear best fits of the calculated values.

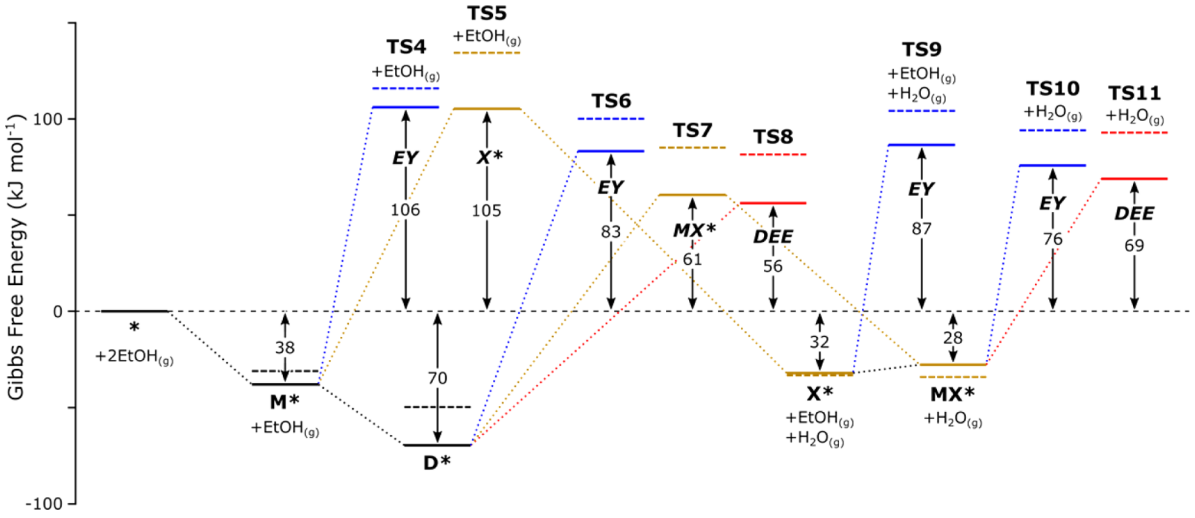

Figure 9. Gibbs free energy diagram for direct EY formation (TS4 and TS6 for monomolecular and bimolecular routes; Figure 5), direct DEE formation (TS8; Figure 7), and ethoxide formation (TS5 and TS7 for monomolecular and bimolecular routes, respectively; Figure 7) from adsorbed ethanol monomers (M*; Figure 3) or protonated EtOH dimers (D*; Figure 3) and sequential EY formation (TS9 and TS10 for monomolecular and bimolecular routes; Figure 5) and sequential DEE formation (TS11; Figure 7) from ethoxides (X*; Figure 3) or EtOH/ethoxide site pairs (MX*; Figure 3) on $H_3PW_{12}O_{40}$ (solid lines) and $H_6CoW_{12}O_{40}$ (dashed lines) at 409 K and standard pressure for all gaseous species.

elementary steps for the formation of EY and DEE from EtOH and reported DFT-derived estimates for the enthalpies and entropies of the intermediates and transition states involved. Next, we rigorously compare the contributions of each of these routes and species to EY and DEE formation at relevant reaction conditions on solid acid catalysts with a broad range of acid strength using rate sensitivity and coverage analysis protocols[66,67] instead of the mere visual inspection of reaction coordinate energy diagrams.

The contribution of an elementary step to the rate at which a given product forms (r_i) can be determined for a given condition by evaluating the fractional change in r_i caused by a small fractional change in the magnitude of the DFT-derived rate constant for the elementary step (k_j)

$$F_{ij} = \frac{\partial \ln r_i}{\partial \ln k_j} \tag{12}$$

An elementary step is inconsequential for forming all (n) products (and can thus be excluded from a sequence) when its overall rate sensitivity coefficient (V_j)

$$V_j = \left(\sum_{i=1}^{n} F_{ij}^2\right)^{1/2} \tag{13}$$

is smaller than a specified threshold at all conditions of interest. Here, the contributions to DEE and EY formation rates by each elementary step in Scheme 1 (Steps 4−11) are determined on each POM acid using eqs 12 and 13 at 0.1−10 kPa EtOH, 0

DOI: 10.1021/acs.jpcc.5b11127
J. Phys. Chem. C 2016, 120, 3371−3389

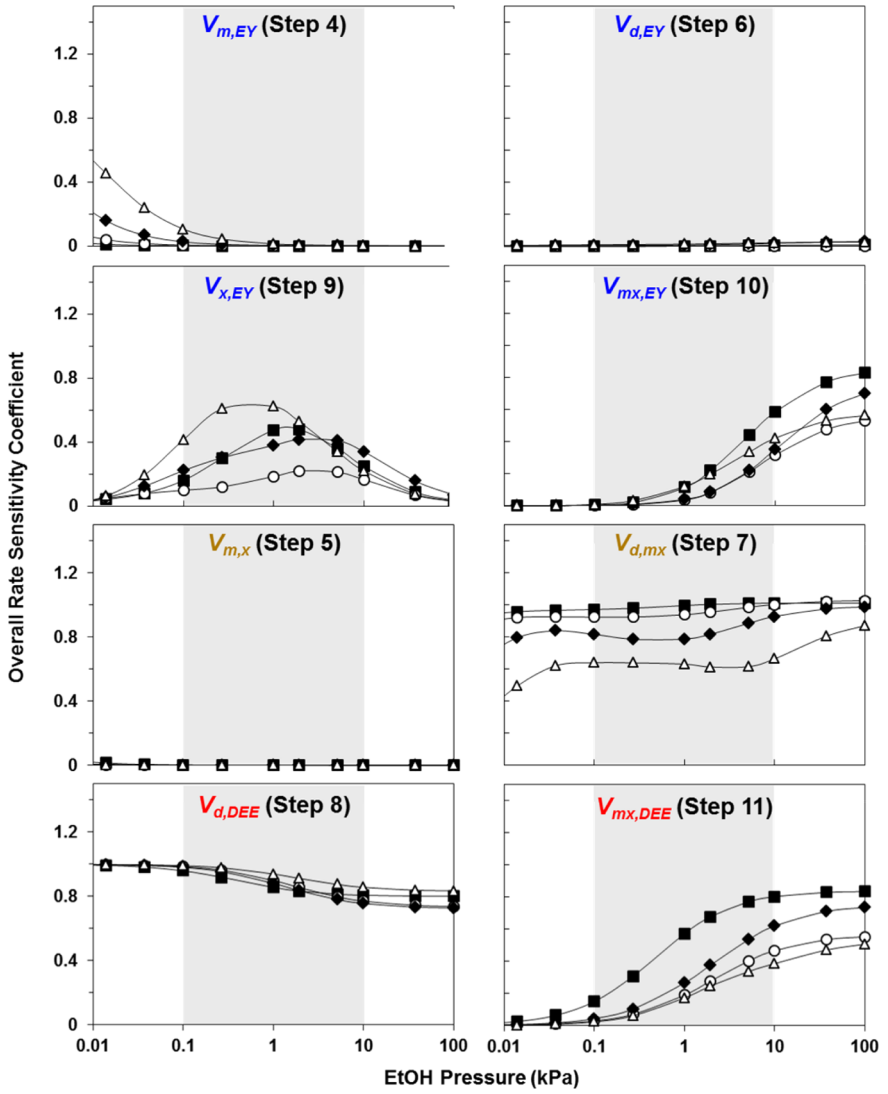

Figure 10. Overall rate sensitivity coefficients (eq 13) as a function of EtOH pressure for the irreversible steps in Scheme 1: direct monomolecular EY formation (Step 4; $V_{m,EY}$), direct bimolecular EY formation (Step 6; $V_{d,EY}$), sequential monomolecular EY formation (Step 9; $V_{x,EY}$), sequential bimolecular EY formation (Step 10; $V_{mx,EY}$), monomolecular ethoxide formation (Step 5; $V_{m,x}$), bimolecular ethoxide formation (Step 7; $V_{d,EY}$), direct DEE formation (Step 8; $V_{d,DEE}$), and sequential DEE formation (Step 11; $V_{mx,DEE}$) on $H_3PW_{12}O_{40}$ (■), $H_4SiW_{12}O_{40}$ (○), $H_5AlW_{12}O_{40}$ (◆), and $H_6CoW_{12}O_{40}$ (△) clusters at 409 K. Shaded regions show range of EtOH pressures considered (0.1−10 kPa) during rate sensitivity analysis.

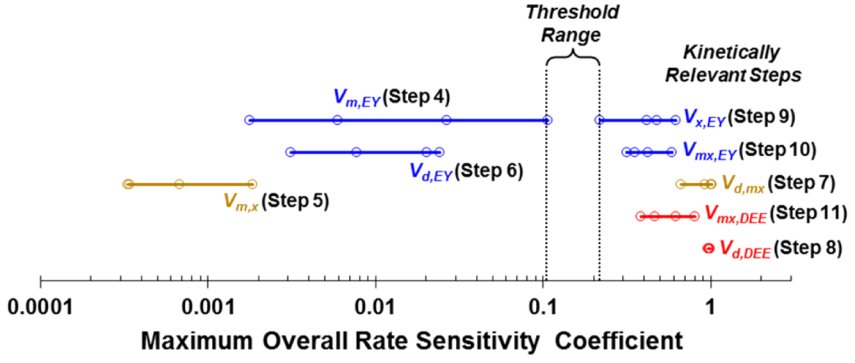

Figure 11. Maximum overall rate sensitivity coefficient for the irreversible steps in Scheme 1 within the considered EtOH pressure range (0.1−10 kPa) on $H_3PW_{12}O_{40}$, $H_4SiW_{12}O_{40}$, $H_5AlW_{12}O_{40}$, and $H_6CoW_{12}O_{40}$ clusters at 409 K.

kPa H_2O (valid at differential conversions), and 409 K. DEE and EY formation rates are calculated from eqs 6−9 with kinetic and thermodynamic constants calculated from DFT-derived Gibbs free energies.

Figure 10 shows V_j values for the rate constants for Steps 4−11 in Scheme 1 at each EtOH pressure on $H_{8-n}X^{n+}W_{12}O_{40}$ clusters (X^{n+} = P^{5+}, Si^{4+}, Al^{3+}, and Co^{2+}). The rate constants for Steps 4, 5, and 6 in Scheme 1 give V_j values below 0.11 at all

DOI: 10.1021/acs.jpcc.5b11127
J. Phys. Chem. C 2016, 120, 3371−3389

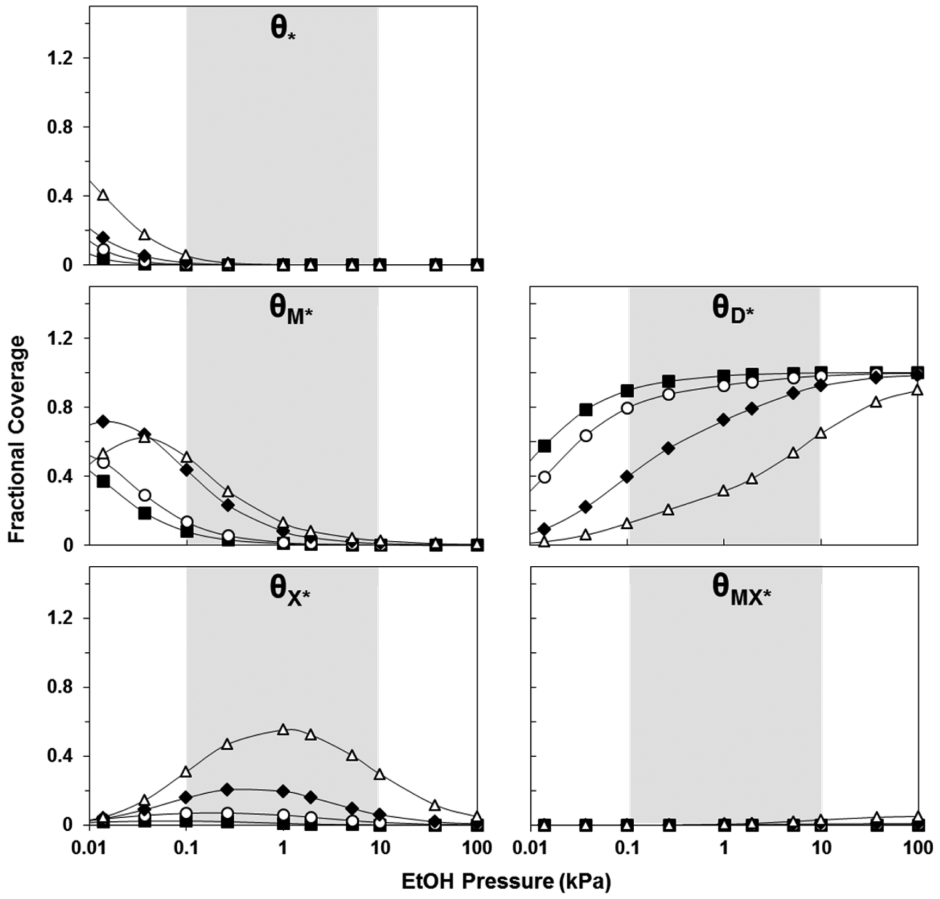

Figure 12. Calculated fractional coverages as functions of EtOH pressure for the surface intermediates considered in the mechanism in Scheme 1: bare protons (θ_*), EtOH monomers (M*; θ_{M*}), protonated EtOH dimers (D*; θ_{D*}), ethoxides (X*; θ_{X*}), and ethoxide/EtOH site pairs (MX*; θ_{MX*}) on $H_3PW_{12}O_{40}$ (■), $H_4SiW_{12}O_{40}$ (○), $H_5AlW_{12}O_{40}$ (◆), and $H_6CoW_{12}O_{40}$ (△) clusters at 409 K. Shaded regions show the range of EtOH pressures considered during coverage analysis.

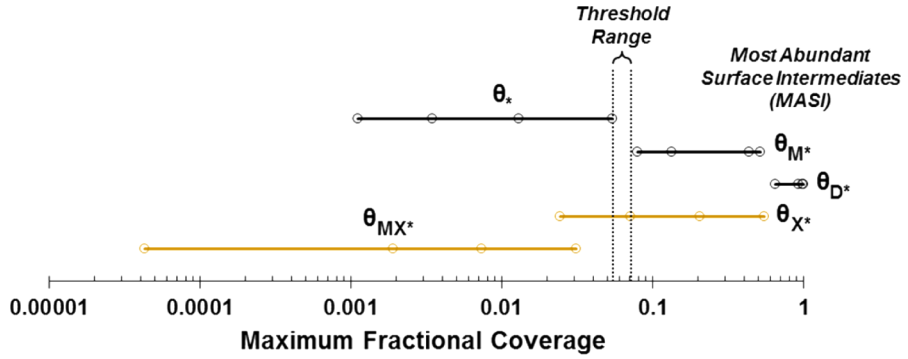

Figure 13. Maximum fractional coverage for the surface intermediates in Scheme 1 within the considered range of EtOH pressure (0.1−10 kPa) on $H_3PW_{12}O_{40}$, $H_4SiW_{12}O_{40}$, $H_5AlW_{12}O_{40}$, and $H_6CoW_{12}O_{40}$ clusters at 409 K.

pressures (0.1−10 kPa) on all POM acids (Figure 11); the rate constants for Steps 7−11 give V_j values above 0.22 at some or all EtOH pressures (Figure 11), suggesting a value of 0.11 as a reasonable threshold V_j value. Using this V_j value, direct monomolecular EY formation (Step 4; $V_{m,EY}$, TS4), monomolecular ethoxide formation (Step 5; $V_{m,x}$, TS5), and direct bimolecular EY formation (Step 6; $V_{d,EY}$, TS6) would not contribute to EY or DEE formation. Therefore, only Steps 1−3 and 7−11 are retained in describing the rate and selectivity data in Figure 2. Next, estimates of the prevalent coverages of all bound species are used to assess the contributions of each of the denominator terms in eqs 6 and 7.

The fractional coverage of a given bound intermediate j (θ_j) is defined as the number of sites occupied by that intermediate ($[B_j]$) divided by the total number of sites ($[H^+]$)

$$\theta_j = \frac{[B_j]}{[H^+]} \tag{14}$$

Values of θ_j much smaller than unity indicate that the denominator term in eq 6 that accounts for its coverage can be neglected in the rate equation, without any associated

DOI: 10.1021/acs.jpcc.5b11127
J. Phys. Chem. C 2016, 120, 3371−3389

implications for the involvement of such intermediates in EY and DEE formation rates. Here, fractional coverages of the surface intermediates in Scheme 1 (bare protons (*), EtOH monomers (M*), protonated EtOH dimers (D*), ethoxides (X*), and EtOH/ethoxide pairs (MX*)) on each of the POM clusters are evaluated at a wide range of EtOH pressures and 409 K.

Values of θ_j from eq 14, the steps in Scheme 1, and DFT-derived free energies are shown in Figure 12 as a function of EtOH pressure for $H_{8-n}X^{n+}W_{12}O_{40}$ clusters (X^{n+} = P^{5+}, Si^{4+}, Al^{3+}, and Co^{2+}). The θ_j values for bare protons and MX* are smaller than 0.06 at all relevant EtOH pressures (0.1−10 kPa) on all POM acids, while X*, M*, and D* give θ_j values larger than 0.07 at most EtOH pressures (0.1−10 kPa) on most POM acids (Figure 13), suggesting a threshold θ_j of 0.06 and leading us to consider only EtOH monomers (M*), protonated EtOH dimers (D*), and ethoxides (X*) as most abundant surface intermediates (MASI). The steps retained from Scheme 1 by the sensitivity analysis and the MASI identified by the coverage analysis can then be used to simplify the equations for EtOH dehydration rates and (DEE/EY) ratios (r_{DEE}/r_{EY}) and to compare their functional form with that inferred from the rate and selectivity data in Figure 2.

3.2.6. Simplified Rate Expressions for Total Ethanol Dehydration Rates and for the Ratio of Diethyl Ether and Ethylene Formation Rates. The elementary steps depicted in Scheme 1, the results of the rate sensitivity analysis, and the assumptions of quasi-equilibrated EtOH physisorption at H^+ and O atoms vicinal to ethoxides or EtOH monomers (Steps 1−3) and irreversible elimination and substitution steps (Steps 7−11) give an expression for the ratio of DEE and EY formation rates (r_{DEE}/r_{EY})

$$\frac{r_{DEE}}{r_{EY}} = \chi + \frac{(1+\chi)\delta\alpha[EtOH]}{1+\alpha[EtOH]}$$

$$\alpha = \frac{k_{mx,EY}K_{MX}}{k_{x,EY}} \quad \chi = \frac{k_{d,mx}}{k_{d,DEE}} \quad \delta = \frac{k_{mx,DEE}}{k_{mx,EY}} \qquad (15)$$

These rates depend on three parameters:

(i) α (kPa^{-1}): the ratio of rate constants for sequential bimolecular EY formation with respect to ethoxides (Steps 3 and 10; $k_{mx,EY}K_{MX}$) and sequential monomolecular EY formation (Step 9; $k_{x,EY}$);

(ii) δ: the ratio of rate constants for sequential bimolecular DEE formation (Step 11; $k_{mx,DEE}$) and sequential bimolecular EY formation (Step 10; $k_{mx,EY}$); and

(iii) χ: the ratio of the rate constants for bimolecular ethoxide formation (Step 7; $k_{d,mx}$) to that for direct DEE formation (Step 8; $k_{d,DEE}$).

The similar r_{DEE}/r_{EY} values on H_nXW/SiO_2 of very different acid strength at all EtOH pressures (Figure 2b) reflect α, δ, and χ values that do not depend on POM composition or acid strength. Therefore, one value for each of these three parameters is regressed from the data in Figure 2b using the functional form of eq 15 (dashed line; Figure 2b); their values are shown in Figure 14 (as dotted lines).

The additional assumptions of pseudo-steady-state for all bound species and of ethoxides, EtOH monomers, and protonated EtOH dimers as MASI give an equation for EtOH dehydration rates

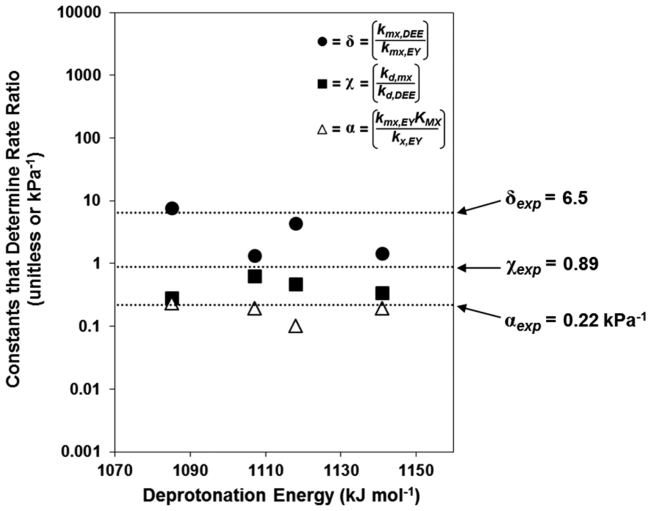

Figure 14. Values of δ (unitless; ●), χ (unitless; ■), and α (kPa^{-1}; △) (for associated steps see the mechanism in Scheme 1) predicted from DFT-derived energies as functions of DPE for $H_{8-n}X^{n+}W_{12}O_{40}$ (X^{n+} = P^{5+}, Si^{4+}, Al^{3+}, and Co^{2+}) catalysts at 409 K. Dotted lines are the values of the ratios derived from the regression of experimental data (Figure 2b) to the functional form of eq 15.

$$\frac{r_{total}}{[H^+]} = \frac{k_{d,mx}(1+\chi)K_D[EtOH]}{1+\left(1+\frac{\phi}{1+(1+\delta)\alpha[EtOH]}\right)K_D[EtOH]}$$

$$\phi = \frac{k_{d,mx}}{k_{x,EY}} \qquad (16)$$

that depends on three additional parameters

(i) $k_{d,mx}$ (ks^{-1}): the rate constant for bimolecular ethoxide formation (Step 7);

(ii) K_D (kPa^{-1}): the equilibrium constant for protonated EtOH dimer formation from EtOH monomers and EtOH(g) (Step 2); and

(iii) ϕ: the ratio of rate constants for bimolecular ethoxide formation (Step 7; $k_{d,mx}$) and sequential monomolecular EY formation (Step 9; $k_{x,EY}$).

The terms in the denominator of eq 16 reflect (from left to right) the relative coverages of EtOH monomers (M*), protonated EtOH dimers (D*), and ethoxides (X*) at acid sites. The dashed lines in Figure 2a represent the regression of all rate data to the functional form of eq 16, using the same values of the three parameters in eq 15 for all acids (dotted lines; Figure 14) and allowing the three parameters in eq 16 to differ among the catalysts if so required in the regression. The regressed values of $k_{d,mx}$, K_D, and ϕ are shown in Figure 15a for H_nXW/SiO_2 samples (X = P, Si, Al, and Co).

Next, these parameters, derived from rate and selectivity data, are compared with those derived from DFT estimates of Gibbs free energies. The observed and predicted effects of acid strength on their values are discussed in the context of differences in charge among the different species involved in the steps accounting for the groupings of thermodynamic and kinetic rate constants that define the parameters in eqs 15 and 16.

3.3. Comparison of Experiment and Theory and the Consequences of POM Composition and Acid Strength.

3.3.1. Ratios of Rates of DEE and EY Formation. Each of the three parameters that determine r_{DEE}/r_{EY} values (eq 14)

DOI: 10.1021/acs.jpcc.5b11127
J. Phys. Chem. C 2016, 120, 3371−3389

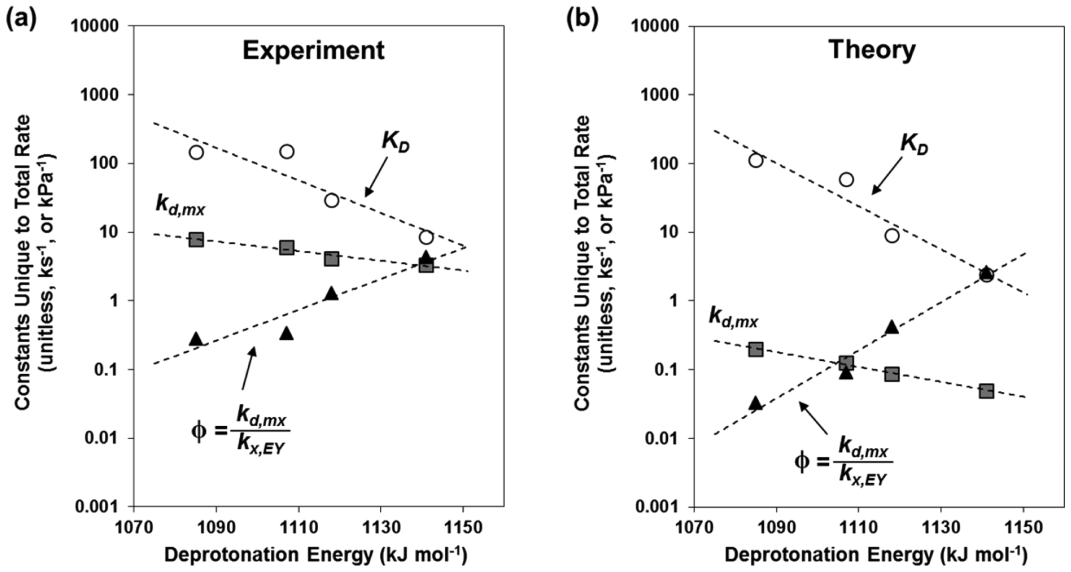

Figure 15. Values of $k_{d,mx}$ (ks^{-1}; gray box), K_D (kPa^{-1}; ○), and ϕ (unitless; ▲) derived from (a) the regression of experimental data for H_nXW/SiO_2 catalysts (X = P, Si, Al, and Co; Figure 2a) to the functional form of eq 16 and from (b) DFT-derived energies for $H_{8-n}X^{n+}W_{12}O_{40}$ clusters (X^{n+} = P^{5+}, Si^{4+}, Al^{3+}, and Co^{2+}) as functions of DPE at 409 K. Dashed lines are best fits of the calculated values.

depends on the ratio of constants for routes from a given intermediate (D* for $k_{d,mx}$ and $k_{d,DEE}$, MX* for $k_{mx,DEE}$ and $k_{mx,EY}$, and X* for $k_{mx,EY}K_{MX}$ and $k_{x,EY}$; Scheme 1). As a result, these ratios, and thus selectivities, reflect differences in free energy between the two TS structures that define each ratio and are unaffected by the stability of their common precursor

$$RT\ \ln\left(\frac{k_{A\to B}}{k_{A\to C}}(\text{bar}^{-\lambda})\right) = G^{\ddagger}_{A\to C} - G^{\ddagger}_{A\to B} - \lambda\cdot G_{EtOH(g)} \tag{17}$$

where $k_{A\to B}$ and $k_{A\to C}$ are rate constants for the two competing routes in each ratio; $G^{\ddagger}_{A\to B}$ and $G^{\ddagger}_{A\to C}$ are the free energies of the respective transition states; λ is the difference in the number of EtOH(g) in the two transition states; and $G_{EtOH,g}$ is the free energy of an EtOH(g) molecule.

The value of α reflects the relative free energies of TS9 (Step 9) and TS10 (Step 10) with a λ value of −1 (TS9 has one more EtOH(g) than TS10). The value of α regressed from measurements on POM/SiO_2 catalysts (0.22 kPa^{-1}; Figure 14) is within the range of values estimated from DFT (0.10−0.24 kPa^{-1}; Figure 14); thus, Steps 9 and 10 become equal in rate at 4.6 kPa EtOH (experiment) and 4.2−9.7 kPa EtOH (theory, range for different POM), and Step 10 becomes the preferred route at the higher EtOH pressures typical of commercial practice.

The value of χ reflects the relative free energies of TS8 (Step 8) and TS7 (Step 7) with a λ value of zero. It is near unity on all POM/SiO_2 acids (0.89; Figure 14), indicative of TS7 and TS8 structures of similar free energies and leading to similar barriers for bimolecular ethoxide formation (Step 7) and direct DEE formation (Step 8). The measured χ value is in reasonable agreement with DFT estimates (0.28−0.64; Figure 14). These two transition states (TS7 and TS8 in Figure 7) contain the same molecular fragments (ethyl, H_2O, and EtOH) but in different geometric alignment. In TS7, the displaced H_2O is H-bonded to the O atom in EtOH, and a POM terminal O atom interacts with the α-carbon in the ethyl fragment. In contrast, the displaced H_2O in TS8 is H-bonded to a terminal O atom in the POM and the O atom in EtOH and interacts with the C_α in the ethyl fragment. The similar free energies of TS7 and TS8 indicate that terminal O atoms in POM acids, and O atoms in EtOH behave similarly when either interacts with the α-carbon of an ethyl fragment or with an H atom in H_2O.

The δ value reflects the relative free energies of TS10 (Step 10) and TS11 (Step 11) with a λ of zero. Its measured value is 6.5 on H_nXW/SiO_2 acids (Figure 14). Thus, TS11 has a slightly lower free energy than TS10 and consequently lower barriers for sequential DEE formation (Step 11) than for sequential bimolecular EY formation (Step 10). DFT-derived δ values are 1.3−7.6 (Figure 14), in reasonable agreement with measurements. The variability of δ values among the POM clusters is equivalent to DFT-derived free energy differences that vary by less than 3 kJ mol^{-1} from their average; this range of δ values, as opposed to the single δ value predicted from experiments, is attributed to the inherent inaccuracies of theoretical treatments. These results suggest that O atoms in EtOH are only slightly better as nucleophiles (for DEE formation; TS11) than as H^+ abstractors (for EY formation; TS10) in reactions with ethoxides.

DFT-derived enthalpies for TS7, TS8, TS9, TS10, and TS11 depend similarly on DPE (dH/dDPE = 0.39−0.52; Table 5), consistent with the significant cationic character for the organic moieties at each of these ion-pair transition states (0.530−0.808; Table 3 and Table 4). These TS enthalpies all increase with increasing DPE (Figure 6 and Figure 8) because both protons and ion-pair transition states benefit from the more stable conjugate bases in stronger POM acids. In contrast, r_{DEE}/r_{EY} ratios are not sensitive to DPE because both transition states in each ratio of rate constants benefit to the same extent from more stable conjugate anions. The unexpected r_{DEE}/r_{EY} trends observed experimentally on these POM acids (Figure 2b), which first motivated our re-examination of plausible alcohol dehydration pathways on Brønsted acids, are well described by eq 15 and give constants in excellent agreement with those obtained from DFT-derived free energies. These findings indicate that that these selectivity trends reflect the contributions of bimolecular routes to ethoxide formation,

DOI: 10.1021/acs.jpcc.5b11127
J. Phys. Chem. C 2016, 120, 3371−3389

Table 5. Dependences of Calculated Enthalpies and Entropies for Surface Intermediates and TS Relative to Bare Protons on Deprotonation Energies (dH/dDPE and dST/dDPE) for $H_{8-n}X^{n+}W_{12}O_{40}$ (X^{n+} = P^{5+}, Si^{4+}, Al^{3+}, and Co^{2+}) Catalysts at 409 K

species[a]	dH/dDPE	dST/dDPE
EtOH monomer (M*)	0.20 ± 0.01	0.08 ± 0.04
protonated EtOH dimer (D*)	0.42 ± 0.04	0.06 ± 0.04
ethoxide (X*)	0.03 ± 0.06	0.07 ± 0.04
bimolecular ethoxide formation (TS7)	0.52 ± 0.04	0.07 ± 0.03
direct DEE formation (TS8)	0.51 ± 0.04	0.06 ± 0.04
sequential monomolecular EY formation (TS9)	0.39 ± 0.02	0.08 ± 0.03
sequential bimolecular EY formation (TS10)	0.41 ± 0.06	0.08 ± 0.03
sequential DEE formation (TS11)	0.50 ± 0.07	0.08 ± 0.03

[a]Labels correspond to structures in Figure 3, Figure 5, or Figure 7.

direct and sequential routes to DEE formation, and sequential monomolecular and bimolecular routes to EY formation.

3.3.2. Combined EtOH Dehydration Rates to EY and DEE. Figure 15a shows measured $k_{d,mx}$, K_D, and ϕ values (obtained by regressing the data in Figure 2a to the form of eq 16) as a function of the DPE values of H_nXW/SiO_2 with P, Si, Al, and Co central atoms. The $k_{d,mx}$ value reflects the free energy barrier for Step 7 (Scheme 1; free energy difference between TS7, for bimolecular ethoxide formation, and D*, a protonated EtOH dimer). Measured $k_{d,mx}$ values (3.3−8.0 ks^{-1}; Figure 15a) are larger than those calculated from DFT-derived free energies (0.05−0.20 ks^{-1}; Figure 15b); these differences correspond to DFT-derived free energy barriers that are 12.6−14.8 kJ mol^{-1} larger than measured values and appear to reflect approximation methods for calculating entropies of low vibrational modes of weakly bound intermediates that underestimate TS7 entropies relative to those for protonated EtOH dimers (D*). The $k_{d,mx}$ values decrease exponentially with increasing DPE, but they reflect an increase in activation barriers much smaller than the concomitant changes in DPE; such attenuation effects[20,36] arise from TS7 structures that benefit from a more stable conjugate anion only slightly more than D*, a conclusion consistent with the similar positive charges at the TS7 cation (0.653−0.680; Table 4) and D* (0.701−0.776; Table 2) and with DFT-derived enthalpies of their formation from bare clusters that depend similarly on DPE (dH/dDPE = 0.42−0.52; Table 5).

The K_D values reflect free energy differences between a protonated EtOH dimer (D*) and an EtOH monomer (M*) and an EtOH(g) molecule (Step 2, Scheme 1). Measured K_D values are larger than unity on POM acids (6.5−156 kPa^{-1}; Figure 15a) and similar to those from DFT-derived free energies (2.4−112 kPa^{-1}; Figure 15b). Measured and DFT-derived K_D values decreased with increasing DPE because protonated EtOH dimers (D*) exhibit larger partial charges than EtOH monomers (0.701−0.776 for D* vs 0.539−0.568 for M* on POM clusters with different central atoms; Table 2); therefore, they benefit from the more stable conjugate anions on stronger acids more than EtOH monomers.

The value of ϕ reflects differences in free energy barriers between Step 7 (D* to TS7) and Step 9 (X* to TS9). Measured ϕ values (0.3−4.3; Figure 15a) are somewhat larger than estimates from DFT-derived free energies (0.03−2.6; Figure 15b). Measurements and theory give ϕ values that increase with increasing DPE (Figure 15), indicating that activation barriers for Step 7 are less sensitive than those for Step 9 to acid strength. The larger ϕ values on weaker acids reflect protonated EtOH dimers (D*) whose stability depends on DPE more sensitively than for ethoxides (X*), while TS7 and TS9 depend similarly on acid strength. These trends are consistent with the larger positive charges in D* than ethoxides (0.701−0.776 for D* vs 0.332−0.350 for X* on POM clusters with different central atoms; Table 2).

Measured rates and (DEE/EY) selectivity ratios are well described by eqs 15 and 16 (dashed lines; Figure 2). The regressed rate and equilibrium constants agree well with those obtained from DFT-derived free energies (Figure 14 and Figure 15) and resolve long-standing uncertainties surrounding the mechanism for ethanol dehydration reactions on Brønsted acids. We expect these kinetically relevant routes and MASI to be valid in general for alkanol dehydration reactions on solid Brønsted acid catalysts, with the identity of the alcohol or the Brønsted acid only affecting the relative contributions of the elementary steps or the relative coverages of surface intermediates. With dehydration rates for other alcohols still reflecting alcohol monomers, protonated alcohol dimers, and alkoxides as MASI, reflect a bimolecular route for alkoxide formation, direct and sequential routes for ether formation, and (for C2 alcohols and above) sequential monomolecular and bimolecular routes for alkene formation. The approach described here also demonstrates how the enumeration of plausible steps, DFT-derived estimates of their dynamics and thermodynamics, and sensitivity analysis methods is a more rigorous framework for determining the relevant steps and species in complex mechanisms than their determination via mere visual inspection of reaction coordinate energy diagrams.

4. CONCLUSIONS

In this study, the elementary steps for alkanol dehydration reactions to alkenes and ethers on solid Brønsted acid catalysts were identified through theoretical investigations of EtOH dehydration reactions on several Brønsted acids of known structure and a broad range of acid strength. The elementary steps in all plausible dehydration routes were enumerated and evaluated based on their respective contributions to product formation rates (predicted from DFT-derived free energies) using protocols based on sensitivity and rate of production analyses that allow quantitative comparisons among routes. The full mechanism was modified to retain only those steps and surface intermediates that are consequential for product formation at conditions relevant to the practice of catalytic dehydration. Experimental rate and rate−ratio data were well described by the simplified mechanism and gave rate and equilibrium constants in good agreement with those obtained from DFT-derived free energies, demonstrating the usefulness of the systematic protocols used for identifying relevant elementary steps and prevalent bound intermediates and validating the proposed simplified mechanism.

H-bonded monomers, protonated alkanol dimers, and alkoxides are the prevalent bound intermediates at conditions relevant to the practice of dehydration catalysis. Direct and sequential routes contribute to ether formation via S_N2-type reactions, with the O atoms in alkanols acting as nucleophiles in attacking the α-carbon in either protonated monomers (direct routes) or alkoxides (sequential routes), displacing a H_2O or a surface O atom, respectively. Alkenes form preferentially via sequential routes involving *syn*-E2-type eliminations, with the C−O bond in alkoxides cleaving while its β-hydrogen is

DOI: 10.1021/acs.jpcc.5b11127
J. Phys. Chem. C 2016, 120, 3371−3389

abstracted by an O atom at either the solid acid surface (monomolecular routes) or at a vicinal physisorbed alkanol (bimolecular routes). Alkoxide formation involves S_N2-type substitutions, with O atoms on surfaces acting as nucleophiles in attacking the α-carbon in protonated monomers and displacing a H_2O molecule, while a second physisorbed alkanol forms hydrogen bonds with the leaving H_2O and a surface O atom. Favorable bimolecular routes for alkene and alkoxide formation demonstrate the profound effects spectator molecules can have on transition state stability, when their presence leads to the formation of strong H-bonds between cationic moieties and negatively charged surface O atoms.

Total dehydration rates increase with increasing acid strength on POM clusters (H_nXW/SiO_2) with different central atoms (X = P, Si, Al, and Co) because the ion-pair transition states that mediate kinetically relevant dehydration steps benefit more than their relevant precursors from the more stable conjugate anions in stronger acids (with lower DPE). Dehydration selectivities, however, are independent of POM composition because the elementary steps that contribute to EY and DEE formation from EtOH are all mediated by ion-pair transition states that exhibit a similar amount and distribution of charge.

■ ASSOCIATED CONTENT

Supporting Information

The Supporting Information is available free of charge on the ACS Publications website at DOI: 10.1021/acs.jpcc.5b11127.

Space velocity effects on measured rate ratios and total dehydration rates. Summary of calculated enthalpies and entropies for TS and intermediates in Scheme 1 (PDF)

■ AUTHOR INFORMATION

Corresponding Author

*Fax: + 1 510-642-4778. E-mail: iglesia@berkeley.edu.

Notes

The authors declare no competing financial interest.

■ ACKNOWLEDGMENTS

The support by the Chemical Sciences, Geosciences, Biosciences Division, Office of Basic Energy Sciences, Office of Science, US Department of Energy under grant number DE-AC05-76RL0-1830, is appreciatively acknowledged. Computational facilities were provided by the Environmental Molecular Science Laboratory (EMSL) at Pacific Northwest National Laboratory (PNNL), a DOE Office of Science User Facility, under proposal number 48772, and by the Extreme Science and Engineering Discovery Environment (XSEDE) which is supported by National Science Foundation grant number CHE-140066. The authors thank Dr. Prashant Deshlahra (UC-Berkeley) and Dr. David Hibbitts (UC-Berkeley) for helpful discussions. We also thank Dr. Cindy Yin (UC-Berkeley) and Dr. Stuart Soled (ExxonMobil) for their assistance with the synthesis of unsupported $H_5AlW_{12}O_{40}$.

■ REFERENCES

(1) Sun, J.; Wang, Y. Recent Advances in Catalytic Conversion of Ethanol to Chemicals. *ACS Catal.* **2014**, *4*, 1078−1090.

(2) Kaplan, S. *Monthly Energy Review October 2015*; 2015.

(3) Phillips, C. B.; Datta, R. Production of Ethylene from Hydrous Ethanol on H-ZSM-5 under Mild Conditions. *Ind. Eng. Chem. Res.* **1997**, *36*, 4466−4475.

(4) Varisli, D.; Dogu, T.; Dogu, G. Ethylene and Diethyl-Ether Production by Dehydration Reaction of Ethanol over Different Heteropolyacid Catalysts. *Chem. Eng. Sci.* **2007**, *62*, 5349−5352.

(5) Fan, D.; Dai, D. J.; Wu, H. S. Ethylene Formation by Catalytic Dehydration of Ethanol with Industrial Considerations. *Materials* **2013**, *6*, 101−115.

(6) Corma, A. Inorganic Solid Acids and Their Use in Acid-Catalyzed Hydrocarbon Reactions. *Chem. Rev.* **1995**, *95*, 559−614.

(7) Takahara, I.; Saito, M.; Inaba, M.; Murata, K. Dehydration of Ethanol into Ethylene over Solid Acid Catalysts. *Catal. Lett.* **2005**, *105*, 249−252.

(8) Roca, F.; De Mourgues, L.; Trambouze, Y. Catalytic Dehydration of Ethanol over Silica-Alumina. *J. Catal.* **1969**, *14*, 107−113.

(9) Saito, Y.; Niiyama, H. Reaction Mechanism of Ethanol Dehydration On/in Heteropoly Compounds: Analysis of Transient Behavior Based on Pseudo-Liquid Catalysis Model. *J. Catal.* **1987**, *106*, 329−336.

(10) Figueras, F.; Trambouze, Y.; Mourgues, L. D. E. Catalytic Dehydration of Ethanol over Silica-Alumina. *J. Catal.* **1969**, *113*, 107−113.

(11) Chiang, H.; Bhan, A. Catalytic Consequences of Hydroxyl Group Location on the Rate and Mechanism of Parallel Dehydration Reactions of Ethanol over Acidic Zeolites. *J. Catal.* **2010**, *271*, 251−261.

(12) Ali, T. T.; Al-Thabaiti, S. a.; Alyoubi, a. O.; Mokhtar, M. Copper Substituted Heteropolyacid Catalysts for the Selective Dehydration of Ethanol. *J. Alloys Compd.* **2010**, *496*, 553−559.

(13) Okuhara, T.; Arai, T.; Ichiki, T.; Lee, K. Dehydration Mechanism of Ethanol in the Pseudoliquid Phase of H3-xCsxPW12O40. *J. Mol. Catal.* **1989**, *55*, 293−301.

(14) de las Pozas, C.; Lopez-Cordero, R.; Gonzalez-Morales, J. A.; Travieso, N.; Roque-Malherbe, R. Effect of Pore Diameter and Acid Strength in Ethanol Dehydration on Molecular Sieves. *J. Mol. Catal.* **1993**, *83*, 145−156.

(15) Gracey, B. P.; Gracey, B. P. Process for Preparing Ethene. US 8,822,748 B2, September 2, 2014.

(16) Bailey, C.; Bolton, L. W.; Gracey, B. P.; Lee, M. K.; Partington, S. R. Process for Producing Olefins. US8440873, 2013.

(17) Partington, S. R. A Process for the Dehydration of Ethanol to Produce Ethene. US20120165589 A1, 2012.

(18) Macht, J.; Janik, M. J.; Neurock, M.; Iglesia, E. Mechanistic Consequences of Composition in Acid Catalysis by Polyoxometalate Keggin Clusters. *J. Am. Chem. Soc.* **2008**, *130*, 10369−10379.

(19) Macht, J.; Janik, M. J.; Neurock, M.; Iglesia, E. Catalytic Consequences of Composition in Polyoxometalate Clusters with Keggin Structure. *Angew. Chem., Int. Ed.* **2007**, *46*, 7864−7868.

(20) Janik, M. J.; Macht, J.; Iglesia, E.; Neurock, M. Correlating Acid Properties and Catalytic Function: A First-Principles Analysis of Alcohol Dehydration Pathways on Polyoxometalates. *J. Phys. Chem. C* **2009**, *113*, 1872−1885.

(21) Macht, J.; Carr, R. T.; Iglesia, E. Consequences of Acid Strength for Isomerization and Elimination Catalysis on Solid Acids. *J. Am. Chem. Soc.* **2009**, *131*, 6554−6565.

(22) Jones, A. J.; Carr, R. T.; Zones, S. I.; Iglesia, E. Acid Strength and Solvation in Catalysis by MFI Zeolites and Effects of the Identity, Concentration and Location of Framework Heteroatoms. *J. Catal.* **2014**, *312*, 58−68.

(23) Knaeble, W.; Carr, R. T.; Iglesia, E. Mechanistic Interpretation of the Effects of Acid Strength on Alkane Isomerization Turnover Rates and Selectivity. *J. Catal.* **2014**, *319*, 283−296.

(24) Cowan, J.; Hill, C. L.; Reiner, R.; Weinstock, I. Dodecatungstoalumic Acid and Its Monolacunary & Mixed-Addendum Derivatives. *Inorg. Synth.* **2002**, *33*, 18−26.

(25) Baker, L.; Loev, B.; McCutcheon, T. Hydrogen Cycle Cation Exchange for Heteropoly Acids and Salts*. *J. Am. Chem. Soc.* **1950**, *72*, 2374−2377.

(26) Baker, L.; McCutcheon, T. Heteropoly Salts Containing Cobalt and Hexavalent Tungsten in the Anion1. *J. Am. Chem. Soc.* **1956**, *78*, 4503−4510.

DOI: 10.1021/acs.jpcc.5b11127
J. Phys. Chem. C 2016, 120, 3371−3389

(27) Baertsch, C.; et al. Genesis of Brønsted Acid Sites during Dehydration of 2-Butanol on Tungsten Oxide Catalysts. *J. Catal.* **2002**, *205*, 44−57.
(28) Kresse, G.; Furthmüller, J. Efficient Iterative Schemes for Ab Initio Total-Energy Calculations Using a Plane-Wave Basis Set. *Phys. Rev. B: Condens. Matter Mater. Phys.* **1996**, *54*, 11169−11186.
(29) Kresse, G.; Hafner, J. Ab Initio Molecular Dynamics for Liquid Metals. *Phys. Rev. B: Condens. Matter Mater. Phys.* **1993**, *47*, 558−561.
(30) Kresse, G.; Hafner, J. Ab Initio Molecular-Dynamics Simulation of the Liquid-Metal−amorphous-Semiconductor Transition in Germanium. *Phys. Rev. B: Condens. Matter Mater. Phys.* **1994**, *49*, 14251−14269.
(31) Kresse, G.; Furthmüller, J. Efficiency of Ab-Initio Total Energy Calculations for Metals and Semiconductors Using a Plane-Wave Basis Set. *Comput. Mater. Sci.* **1996**, *6*, 15−50.
(32) Blöchl, P. E. Projector Augmented-Wave Method. *Phys. Rev. B: Condens. Matter Mater. Phys.* **1994**, *50*, 17953−17979.
(33) Kresse, G.; Joubert, D. From Ultrasoft Pseudopotentials to the Projector Augmented-Wave Method. *Phys. Rev. B: Condens. Matter Mater. Phys.* **1999**, *59*, 1758−1775.
(34) Perdew, J.; Chevary, J.; Vosko, S.; et al. Atoms, Molecules, Solids, and Surfaces: Applications of the Generalized Gradient Approximation for Exchange and Correlation. *Phys. Rev. B: Condens. Matter Mater. Phys.* **1992**, *46*, 6671−6687.
(35) Monkhorst, H. J.; Pack, J. D. Special Points for Brillouin-Zone Integrations. *Phys. Rev. B* **1976**, *13*, 5188−5192.
(36) Carr, R. T.; Neurock, M.; Iglesia, E. Catalytic Consequences of Acid Strength in the Conversion of Methanol to Dimethyl Ether. *J. Catal.* **2011**, *278*, 78−93.
(37) Deshlahra, P.; Carr, R. T.; Chai, S.-H.; Iglesia, E. Mechanistic Details and Reactivity Descriptors in Oxidation and Acid Catalysis of Methanol. *ACS Catal.* **2015**, *5*, 666−682.
(38) Makov, G.; Payne, M. Periodic Boundary Conditions in Ab Initio Calculations. *Phys. Rev. B: Condens. Matter Mater. Phys.* **1995**, *51*, 4014−4022.
(39) Löwdin, P.-O. On the Non-Orthogonality Problem Connected with the Use of Atomic Wave Functions in the Theory of Molecules and Crystals. *J. Chem. Phys.* **1950**, *18*, 365.
(40) Löwdin, P.-O. On the Nonorthogonality Problem. *Adv. Quantum Chem.* **1970**, *5*, 185−199.
(41) Lu, W. C.; Wang, C. Z.; Schmidt, M. W.; Bytautas, L.; Ho, K. M.; Ruedenberg, K. Molecule Intrinsic Minimal Basis Sets. I. Exact Resolution of Ab Initio Optimized Molecular Orbitals in Terms of Deformed Atomic Minimal-Basis Orbitals. *J. Chem. Phys.* **2004**, *120*, 2629.
(42) Lu, W. C.; Wang, C. Z.; Chan, T. L.; Ruedenberg, K.; Ho, K. M. Representation of Electronic Structures in Crystals in Terms of Highly Localized Quasiatomic Minimal Basis Orbitals. *Phys. Rev. B: Condens. Matter Mater. Phys.* **2004**, *70*, 041101.
(43) Chan, T.-L.; Yao, Y. X.; Wang, C. Z.; Lu, W. C.; Li, J.; Qian, X. F.; Yip, S.; Ho, K. M. Highly Localized Quasiatomic Minimal Basis Orbitals for Mo from Ab Initio Calculations. *Phys. Rev. B: Condens. Matter Mater. Phys.* **2007**, *76*, 205119.
(44) Qian, X.; Li, J.; Qi, L.; Wang, C.-Z.; Chan, T.-L.; Yao, Y.-X.; Ho, K.-M.; Yip, S. Quasiatomic Orbitals for *ab Initio* Tight-Binding Analysis. *Phys. Rev. B: Condens. Matter Mater. Phys.* **2008**, *78*, 245112.
(45) Henkelman, G.; Uberuaga, B. P.; Jónsson, H. Climbing Image Nudged Elastic Band Method for Finding Saddle Points and Minimum Energy Paths. *J. Chem. Phys.* **2000**, *113*, 9901−9904.
(46) Henkelman, G.; Jónsson, H. A Dimer Method for Finding Saddle Points on High Dimensional Potential Surfaces Using Only First Derivatives. *J. Chem. Phys.* **1999**, *111*, 7010.
(47) Hibbitts, D. D.; Jiménez, R.; Yoshimura, M.; Weiss, B.; Iglesia, E. Catalytic NO Activation and NO−H2 Reaction Pathways. *J. Catal.* **2014**, *319*, 95−109.
(48) Campbell, C. T.; Sellers, J. R. V. Enthalpies and Entropies of Adsorption on Well-Defined Oxide Surfaces: Experimental Measurements. *Chem. Rev.* **2013**, *113*, 4106−4135.
(49) Eyring, H. The Activated Complex in Chemical Reactions. *J. Chem. Phys.* **1935**, *3*, 107−115.
(50) Evans, M. G.; Polanyi, M. Some Applications of the Transition State Method to the Calculation of Reaction Velocities, Especially in Solution. *Trans. Faraday Soc.* **1935**, *31*, 875.
(51) Bardin, B. B.; Davis, R. J. Effect of Water on Silica-Supported Phosphotungstic Acid Catalysts for 1-Butene Double Bond Shift and Alkane Skeletal Isomerization. *Appl. Catal., A* **2000**, *200*, 219−231.
(52) Janik, M. J.; Bardin, B. B.; Davis, R. J.; Neurock, M. A Quantum Chemical Study of the Decomposition of Keggin-Structured Heteropolyacids. *J. Phys. Chem. B* **2006**, *110*, 4170−4178.
(53) Rozanska, X.; Sautet, P.; Delbecq, F.; Lefebvre, F.; Borshch, S.; Chermette, H.; Basset, J.-M.; Grinenval, E. Polyoxometalate Grafting onto Silica: Stability Diagrams of H3PMo12O40 on {001}, {101}, and {111} β-Cristobalite Surfaces Analyzed by DFT. *Phys. Chem. Chem. Phys.* **2011**, *13*, 15955−15959.
(54) Alharbi, W.; Brown, E.; Kozhevnikova, E. F.; Kozhevnikov, I. V. Dehydration of Ethanol over Heteropoly Acid Catalysts in the Gas Phase. *J. Catal.* **2014**, *319*, 174−181.
(55) Sun, J.; Wang, Y. Recent Advances in Catalytic Conversion of Ethanol to Chemicals. *ACS Catal.* **2014**, *4*, 1078−1090.
(56) Lee, K. Y.; Arai, T.; Nakata, S.; Asaoka, S.; Okuhara, T.; Misono, M. Catalysis by Heteropoly Compounds. 20. An NMR Study of Ethanol Dehydration in the Pseudoliquid Phase of 12-Tungstophosphoric Acid. *J. Am. Chem. Soc.* **1992**, *114*, 2836−2842.
(57) Kim, S.; Robichaud, D. J.; Beckham, G. T.; Paton, R. S.; Nimlos, M. R. Ethanol Dehydration in HZSM-5 Studied by Density Functional Theory: Evidence for a Concerted Process. *J. Phys. Chem. A* **2015**, *119*, 3604−3614.
(58) Maihom, T.; Khongpracha, P.; Sirijaraensre, J.; Limtrakul, J. Mechanistic Studies on the Transformation of Ethanol into Ethene over Fe-ZSM-5 Zeolite. *ChemPhysChem* **2013**, *14*, 101−107.
(59) John, M.; Alexopoulos, K.; Reyniers, M.-F.; Marin, G. B. Reaction Path Analysis for 1-Butanol Dehydration in H-ZSM-5 Zeolite: Ab Initio and Microkinetic Modeling. *J. Catal.* **2015**, *330*, 28−45.
(60) Pimentel, G. C.; McClellan, A. L. Hydrogen Bonding. *Annu. Rev. Phys. Chem.* **1971**, *22*, 347−385.
(61) Perrin, C. L.; Nielson, J. B. Strong" Hydrogen Bonds in Chemistry and Biology. *Annu. Rev. Phys. Chem.* **1997**, *48*, 511−544.
(62) Pauling, L. *The Nature of the Chemical Bond, An Introduction to Modern Structural Chemistry*, 3rd ed.; Cornell University Press: Ithaca, United States, 1960.
(63) Gronert, S. Theoretical Studies of Elimination Reactions. 1. Reactions of F- and PH2- with CH3CH2Cl. Competition between SN2 and E2Mechanisms for First- and Second-Row Nucleophiles. *J. Am. Chem. Soc.* **1991**, *113*, 6041−6048.
(64) Bunnett, J. F. The Mechanism of Bimolecular β-Elimination Reactions. *Angew. Chem., Int. Ed. Engl.* **1962**, *1*, 225−235.
(65) Bach, R. D.; Badger, R. C.; Lang, T. J. Theoretical Studies on E2 Elimination Reactions. Evidence That Syn Elimination Is Accompanied by Inversion of Configuration at the Carbanionic Center. *J. Am. Chem. Soc.* **1979**, *101*, 2845−2848.
(66) Tomlin, a. S.; Pilling, M. J.; Turanyi, T.; Merkin, J. H.; Brindley, J. Mechanism Reduction for the Oscillatory Oxidation of Hydrogen: Sensitivity and Quasi-Steady-State Analyses. *Combust. Flame* **1992**, *91*, 107−130.
(67) Zeng, G.; Pilling, M. J.; Saunders, S. M. Mechanism Reduction for Tropospheric Chemistry Butane Oxidation. *J. Chem. Soc., Faraday Trans.* **1997**, *93*, 2937−2946.

DOI: 10.1021/acs.jpcc.5b11127
J. Phys. Chem. C 2016, 120, 3371−3389